IJAME

Int. J. of Applied Mechanics and Engineering, 2026, vol.31, No.2, pp.1-30
DOI: 10.59441/ijame/217479

MULTIPLE SLIPS ON BOUNDARY LAYER HYDROMAGNETIC NANOFLUID FLOW THROUGH A CYLINDER WITH MULTIPLE REGRESSION ANALYSIS

U.H. Hani[1], M.A. Ali[1*], and R.N. Nasrin[2]
[1]Mathematics, Chittagong University of Engineering and Technology, BANGLADESH
[2]Mathematics, Bangladesh University of Engineering and Technology, BANGLADESH
E-mail: ali.mehidi93@gmail.com

The complex boundary layer (BL) featuring nanofluid phenomena involving multiple slip conditions, heat-mass transfer, magnetohydrodynamics (MHD), stretching ratio, heat generation, curvature, viscous dissipation, thermal radiation, mixed convection, and chemical reaction through a nonlinear stretching cylindrical surface is investigated by this research. The collection of nonlinear partial differential equations is transformed into ordinary differential equations using a suitable transformation. These resultant equations are resolved using a numerical approach, specifically the shooting method. The novelty of this work lies in the integrated analysis of nanofluid boundary layer flow over a nonlinear cylindrical surface, simultaneously incorporating MHD effects, multiple slip conditions, heat and mass transfer, thermal radiation, viscous dissipation, mixed convection, chemical reactions, and heat generation, while providing both numerical solutions and regression-based predictive insights. The velocity gradient increases by almost *58%*, *56%* and *49%* due to escalating magnetic field, power-law index, and velocity slip, respectively, whereas the Nusselt number increases by almost *39%*, *78%* and *47%* for escalating heat generation, velocity, and thermal slips, respectively. The significant contributing variables for the multiple regression equations of the skin friction, thermal, and material transport rates are calculated. The research findings may have implications for various engineering and industries such as MHD power generators, drug delivery systems, and boundary layer management in aerodynamics, which control and manage velocity-thermal-concentration fields.

Key words: boundary layer, slip conditions, curvature, chemical reaction, shear stress.

1. Introduction

Because of its relevance in fluid dynamics, the boundary layer (BL) has attracted much interest from researchers. Ludwig Prandtl initially suggested the notion of a BL in (Gersten, [1]). The BL theory demonstrates that the surface velocity of a stationary body is zero for a non-slip state. Still, the velocity predicted by the non-viscous flow theory would be obtained inside a thin layer known as the boundary layer. Along with a brief synopsis of Prandtl's work in his pioneering publications, Tulapurkara [2] has discussed some of the developments in boundary layer theory. According to him, the succeeding, quickly developing field of aerodynamics research and its applications relied heavily on Prandtl's boundary layer theory. In addition, it significantly expedited associated breakthroughs in other engineering fields, including mass and heat transfer, hydraulics, turbo machinery design, and fluid flow (Tulapurkara, [2]). Researchers are very interested in boundary layer theory because of its significance in the various fluid flow domains. In the critical subject of fluid dynamics research, the thermal performance of nanofluids in unstable flow has been rigorously investigated by Khan *et al.* [3], focusing on the effects of injection/suction. Both space sciences and aerodynamics make extensive use of this flow scenario. They have used ND-H_2O and Ag-H_2O as nanofluids in their model formulation, doing numerical research and investigating the dynamics of the nanofluids for the impacts of relevant factors. Elbashbeshy *et al.* [4] have examined numerically how heat production and/or absorption affected the nanofluid boundary layer flow carrying gyrotactic microorganisms that transferred mass

* To whom correspondence should be addressed

and heat across an inclined stretched cylinder. They observed that the inclination angle marginally impacted motile microorganisms' temperature, concentration, and velocity. Nanofluids are an innovative class of solid-liquid composite materials consisting of solid nanoparticles dispersed in a base heat-transfer fluid. These nanoparticles typically range in size from *1* to *100* nanometers. Owing to their significantly enhanced thermal properties, nanofluids have recently garnered considerable research interest. For example, the addition of a small amount of copper or carbon nanoparticles can increase the inherently low thermal conductivity of ethylene glycol and oil by approximately *40%* and *150%*, respectively. To produce this kind of augmentation, conventional particle-liquid suspensions need large particle concentrations $(>10\%)$; nevertheless, they are not widely used due to rheological and stability issues (Eastman *et al.* [5]). Among the many advantages of nanofluids are their increased cooling rates, lower wear resistance, smaller and lighter cooling systems, decreased requirement for pumping power, lowered inventory of heat transfer fluids, and decreased friction coefficient. They were intended for engineering applications, such as creating novel coolants and shrinking heat exchangers (Tuckerman and Pease, [6]). The authors believe that this multidisciplinary study on nanofluids offers a fantastic chance to investigate uncharted territory in wet nanotechnology. Considering gold and alumina as nanoparticles, Elgazery [7] has examined two instances of nanofluid in his study: (i) addressed a Newtonian nanofluid in the first instance, using water as the base fluid and Au (gold) or Al_2O_3 (alumina) as nanoparticles. The viscosity coefficient, $\beta \to \infty$, and Prandtl number, $Pr = 6.788$ (for water), are examined in the findings. (ii) investigated a non-Newtonian bio-nanofluid in the second instance, where blood is the base fluid and Au (gold) or Al_2O_3 (alumina) is the nanoparticle. The viscosity coefficient, $\beta = 0.1$, and Prandtl number, $\mathrm{Pr} = 25$ (for blood), are examined in the findings.

Adding additives to base fluids is one way to improve their heat transfer capabilities. Researchers have theoretically and experimentally demonstrated that nanofluids can increase base fluids' thermal conductivity and convective heat transfer performance (Kandasamy, [8]). Higher absorption levels inside the fluid are made possible by including small particles, which scatter incoming radiation. Due to constant collisions between the nanoparticles and the base fluid's molecules, the nanoparticles move randomly throughout the fluid, known as Brownian motion. The development of the general transport model for nanofluid uses the mass flow of nanoparticles, which is attributed to Brownian diffusion. Also, when the temperature gradient is present, particles can spread. Thermophoresis is the term for this phenomenon, which is the particle counterpart of the well-known Soret effect for mixtures of gases or liquids. Thermophoretic processes cause the mass flux of nanoparticles, and the general transport model for nanofluids can be derived based on this phenomenon. The thermal diffusion coefficient describes the thermophoresis. Reddy and Chamkha [9] have quantitatively studied the boundary layer nanofluid flow above a circular cylinder with the effects of thermophoresis and Brownian motion. Mahdy and Chamkha [10] discussed the unsteady two-dimensional nanofluid flow over a contracting cylinder with a combined similarity-numerical approach. They found that the Casson parameter's growing influence caused the suppressed velocity profile. Additionally, they observed that the heat and mass transfer rate decreased with the increase of the time-dependent and Brownian motion parameters.

Prasannakumara [11] has performed the effect of the Cattaneo-Christov model and magnetic dipole over a stretched sheet due to nanofluid flow. To do this, he considered engine oil a base fluid, whereas TC4 (Ti-6Al-4V) was a nanoparticle. He found that Newtonian fluid has superior thermal performance to Maxwell fluid. Numerous studies have examined the nanofluid flow characteristics under various conditions (Bhatti *et al.* [12]; Chamkha *et al.* [13]; Dogonchi *et al.* [14], Reddy *et al.* [15]).

The nanofluid is considered electrically conducting when magnetic nanoparticles are present. Magnetofluid dynamics, hydromagnetics, and MHD are commonly used to describe electrically conducting fluids. Due to its widespread use in geothermal and industrial technologies, MHD absorbs energy and generates a controllable behavior that may be directed and controlled by applying external magnetic fields, according to research by Hussain *et al.* [16,17]. This slows the rate at which the cooled material solidifies and improves its mechanical properties. Using a radially imposed magnetic field, Globe [18] first examined the problem of a steady incompressible flow of two indefinitely along circular cylinders. The effects of heat radiation and a magnetic dipole on a Maxwell nanoliquid flow implanted with SWCNT/MWCNT on a

stretched sheet were investigated by Kumar *et al.* [19]. For the rapid importance of MHD, some research has examined how the magnetic field affects fluid flow problems (Khan *et al.* [20]; Makinde *et al.* [21]; Rashidi *et al.* [22]; Vishnu *et al.* [23, 24]).

Owing to numerous applications of cylindrical surfaces in engineering, modern technology, and industry, numerous researchers have concentrated on studying the flow in the BL and heat transfer through a cylindrical stretched surface. Abbas *et al.* [25] have analysed the MHD BL hybrid nanofluid flow over a spinning cylinder. They found that the heat transfer rate drops when thermal slip levels increase, while skin friction remains constant. Due to the significance of the melting heat transfer, the movement of a dusty nanofluid through an impermeable stretching cylinder has been presented by Umeshaiah *et al.* [26], and they found that increasing the porosity parameter can result in reduced fluid- and dust-phase velocities.

Mixed convection has become an important research field for hydrodynamic researchers due to its importance in enhancing the thermal properties of heat transfer, such as producing float glass, food processing, solar energy storage, electronics cooling, and drying technologies. Alumina and copper nanoparticle-based hybrid nanofluid flow over a horizontal circular cylinder has been studied by EL-Zahar *et al.* [27] using a magneto-mixed approach. They found that Cu-water had the most significant drag coefficient and Nusselt number compared to the hybrid and Al_2O_3-water nanofluid. The drag coefficient's value also decreases as the solid volume portion increases. Pak and Choi [28] have examined the possibility of convective heat transfer in the case of turbulent nanofluid flow regimes. To explore the mixed convective nanofluids flow embedded in a porous medium, Ahmad and Pop [29] employed a vertical flat plate. Numerous studies (RamReddy *et al.*, [30]; Rashad *et al.* [31-33]) are available on the mixed convective flow of nanofluids.

Due to its significance in several practical applications, the interaction between natural convection and heat radiation has seen significant interest during the past few years. When a radiating surface releases thermal radiation, electromagnetic waves are released together with the heat energy. Thermal radiation significantly impacts some technical operations, including high heat, such as re-entering spacecraft and weaponry. A study on the single-phase nanofluid flow with thermal radiation has been conducted by Turkyilmazoglu and Pop [34]. Anwar *et al.* [35] performed a water-based nanofluid flow of Cu and TiO_2 across a vertical plate and found that the thermal profile declines with the heat sink parameter and Prandtl number. Researchers Reddy and Shankar [36] have examined the magnetic field radiative heat transfer effect in a porous medium and time-dependent MHD nanofluid flow through an unbounded flat plate with a ramping temperature gradient. To do this, they have considered two types of nanofluids (water-based) comprising titanium dioxide (TiO_2) and silver (Ag). They found that the heat and velocity profiles rise while the radiation factor increases, but the velocity declines if the magnetic parameter increases.

For various applications, such as thermal insulation, metal casting, geothermal energy, and electrical device cooling, heat transfer is a crucial part of geographical, technological, and industrial processes. Tayabi *et al.* [37] investigated the effects of internal heat generation/absorption processes on thermal-natural convection in a concentric circular annular enclosure split by a conductive material and filled with a hybrid nanofluid. Their study considered Cu and Alumina (Al_2O_3) as the nanoparticles. Researchers have found that the annulus's flow and heat exchange behaviors are significantly altered by the combined impacts of the interior heat generation/absorption phenomena and the combined nanoparticles when a conductive solid barrier is present. Hafeez and Khan [38] have studied the fluid's swirling motion caused by a spinning disk coupled with the viscoelastic Oldroyd-B fluid model. The researchers have considered the Cattaneo-Christov temperature and mass fluctuation theories to investigate the fluid's temperature processes. In their research, they have also regarded chemical reactions and heat generation/absorption. They noticed that as the magnetic parameter increases within a specific range, the Odroyd-B fluid’s temperature increases. Additionally, they detected that the temperature declines as the thermal reduction time parameter rises and that the concentration distribution is impacted by the solutal relaxation time parameter in a declining trend. The impacts of heat generation on the hybrid nanofluid flow (stagnation point) have been investigated by Masood *et al.* [39] by taking polystyrene ($(C_8H_8)_n$) and TiO_2 as nanoparticles. The authors have concentrated their research on stretched surfaces-induced hybrid nanofluid flow. According to the authors, the temperature field increases with the heat generation/absorption coefficient, whereas the velocity field intensifies with the velocity ratio parameter.

The flow analysis comprising a slip boundary is fundamental. In contrast to no-slip boundary conditions, it has become more significant recently, because no-slip is no longer advantageous for processes involving suspensions, polymer solutions, foams where the fluid acts like a particle, emulsions, etc. Because of its broad use, the flow of nanofluids has drawn much interest in studying the issues with partial and full slip boundary conditions. In their publications on the impact of slip in the flow of nanofluid research, early reports of this type of formulation were made by Turkyilmazoglu [40, 41] and Akbar *et al.* [42]. Alongside them, Mustafa and Khan [43] disclosed how slip circumstances relate to convective situations in electrically conducting nanofluid flow toward a stretched disk within a rotational frame. In their study, ferrous-ferric oxide (Fe_3O_4) was considered a kind of nanoparticle. The mixed convective BL nanofluid flow over an exponentially stretched surface has been studied by Mahanthesh *et al.* [44].

Pradhan *et al.* [45] examined the unsteady squeezing flow of a micropolar fluid confined between two parallel disks, incorporating the influences of a transverse magnetic field and a porous medium. Mishra *et al.* [46] investigated the time-dependent magnetized flow of nanomaterials over a rotating and spinning sphere, optimizing the heat transfer rate by incorporating nonlinear radiation, a variable heat source, thermal buoyancy, and a transverse magnetic field. Their results revealed that increasing the concentration of carbon nanotubes reduces the velocity profiles, thereby thickening the boundary layer, whereas stronger magnetization produces the opposite effect. Agbaje *et al.* [47] investigated the irreversibility phenomena in the squeezing flow of a polar hybrid nanofluid, considering blood as the base fluid with copper (Cu) and silver (Ag) nanoparticles, while accounting for dissipative heat effects (viscous and Joule heating) along with thermal radiation. Panda *et al.* [48] examined the flow of a polar nanofluid over a stretching permeable surface, considering Darcy-Forchheimer inertial drag, space- and temperature-dependent heat generation/absorption, thermal radiation, Brownian motion, and thermophoresis. They reported that thermal and solutal buoyancy enhance velocity, while inertial drag reduces it. The heat source elevates temperature, whereas a higher Lewis number significantly decreases fluid concentration.

The current study is connected to earlier investigations that examined the impact of multiple slip impacts on heat and mass transmission in the MHD flow of nanofluid across a stretched cylindrical-shaped geometry. Earlier research has looked at the consequences of several slips on different fluid flow arrangements. This study expands on earlier research and offers critical new understandings of heat transfer processes in intricate fluid flow configurations.

Therefore, this work aims to examine the case of nanofluid flow along cylindrical shape geometry by applying Buongiorno's model, how temperature and concentration transfer phenomena are affected due to thermal radiation, viscous dissipation, multiple slips, chemical reaction, temperature generation/absorption when a magnetic field is present.

2. Mathematical model

This numerical and theoretical study considers a steady, *2* dimensional, incompressible boundary layer nanofluid flow along a cylindrical-shaped surface containing viscous dissipation, thermal radiation, temperature generation/absorption, chemical reaction, and magnetic field. The cylindrical coordinate system (r, θ, z) is adopted with the axisymmetric $\left(\frac{\partial}{\partial \theta} = 0\right)$ flow assumption for the mathematical depiction. The fluid velocities u, and v are considered along the z- and *r*-direction of the cylinder, respectively. The nanofluid flow is considered along the *z*-axis, and the strength of the magnetic field B_0 is acted along the radial direction of the cylinder as displayed in Fig.1. The magneto-Reynolds number is assumed to be small; consequently, the induced magnetic field is neglected. The cylinder is stretched with a stretching velocity $U_w = az^n$, where $a > 0$, the stretching constant, while $U = bz^n$ represents the free stream velocity. In this case, the surface has a variable temperature T_w and a variable concentration C_w, while the surrounding fluid maintains a uniform ambient temperature T_∞ and uniform ambient concentration C_∞, with $T_w > T_\infty$ and $C_w > C_\infty$.

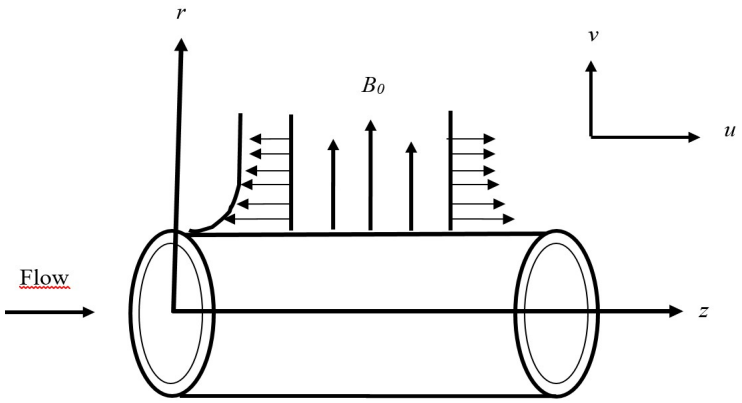

Fig.1. Flow configuration and coordinate system.

The fundamental equations of motion are

$$\frac{\partial \rho}{\partial t} + \nabla \cdot (\rho \boldsymbol{V}) = 0\,, \tag{2.1}$$

$$\rho\left(\frac{\partial \boldsymbol{V}}{\partial t} + \boldsymbol{V} \cdot \nabla \boldsymbol{V}\right) = -\nabla p + \mu \nabla^2 \boldsymbol{V} + \boldsymbol{F}\,, \tag{2.2}$$

$$\rho C_p\left(\frac{\partial T}{\partial t} + \boldsymbol{V} \cdot \nabla T\right) = k\nabla^2 T + \Phi + Q\,, \tag{2.3}$$

$$\frac{\partial C}{\partial t} + \boldsymbol{V} \cdot \nabla C = D\nabla^2 C + R\,. \tag{2.4}$$

Furthermore, the velocity, temperature, and concentration slip effects are considered in convective boundary conditions. Under the above assumptions, the mass, momentum, energy, and concentration equations, respectively, appear as [49]:

$$\frac{\partial u}{\partial z} + \frac{v}{r} + \frac{\partial v}{\partial r} = 0\,, \tag{2.5}$$

$$u\frac{\partial u}{\partial z} + v\frac{\partial u}{\partial r} = U\frac{dU}{dz} + \nu\left(\frac{\partial^2 u}{\partial r^2} + \frac{1}{r}\frac{\partial u}{\partial r}\right) - \frac{\sigma B_0^2}{\rho_f}(u - U) + \beta_T g(T - T_\infty) + \beta_c^* g(C - C_\infty)\,, \tag{2.6}$$

$$\begin{aligned} u\frac{\partial T}{\partial z} + v\frac{\partial T}{\partial r} &= \alpha_r\left(\frac{\partial^2 T}{\partial r^2} + \frac{1}{r}\frac{\partial T}{\partial r}\right) + \tau\left[D_B\frac{\partial C}{\partial r}\frac{\partial T}{\partial r} + \frac{D_T}{T_\infty}\left(\frac{\partial T}{\partial r}\right)^2\right] - \\ &+ \frac{1}{\rho_f C_p r}\frac{\partial (r q_r)}{\partial r} + \frac{Q_0}{\rho_f C_p}(T - T_\infty) + \frac{\nu}{C_p}\left(\frac{\partial u}{\partial r}\right)^2\,, \end{aligned} \tag{2.7}$$

$$u\frac{\partial C}{\partial z} + v\frac{\partial C}{\partial r} = D_B\left[\frac{\partial^2 C}{\partial r^2} + \frac{1}{r}\frac{\partial C}{\partial r}\right] + \frac{D_T}{T_\infty}\left[\frac{\partial^2 T}{\partial r^2} + \frac{1}{r}\frac{\partial T}{\partial r}\right] - K(C - C_\infty)\,. \tag{2.8}$$

The thermal radiative flux (by assuming Roseland's approximation) is considered as [50]:

$$q_r = -\frac{4\sigma^*}{3k^*}\frac{\partial\left(T^4\right)}{\partial r} \tag{2.9}$$

where k^* is the mean absorption coefficient, and σ^* is the Stefan-Boltzmann constant. The nanofluid's temperature is assumed to be related to T_∞^4. Using Taylor series expansion, T^4 can expand about T_∞, and disregarding higher-order terms, one can find

$$T^4 = 4T_\infty^3 T - 3T_\infty^4. \tag{2.10}$$

Interleaving Eq.(2.10) into Eq.(2.9), q_r can be determined as

$$q_r = -\frac{4\sigma^*}{3k^*}\frac{\partial}{\partial r}\left(4T_\infty^3 T\right); \tag{2.11}$$

Then Eq.(2.7) may be transcribed as:

$$\begin{aligned} &u\frac{\partial T}{\partial z} + v\frac{\partial T}{\partial r} = \alpha_r\left(\frac{\partial^2 T}{\partial r^2} + \frac{1}{r}\frac{\partial T}{\partial r}\right) + \tau\left[D_B\frac{\partial C}{\partial r}\frac{\partial T}{\partial r} + \frac{D_T}{T_\infty}\left(\frac{\partial T}{\partial r}\right)^2\right] + \\ &+\frac{16\sigma^* T_\infty^3}{3\rho_f C_p k^*}\left[\frac{\partial^2 T}{\partial r^2} + \frac{1}{r}\frac{\partial T}{\partial r}\right] + \frac{Q_0}{\rho_f C_p}\left(T - T_\infty\right) + \frac{\nu}{C_p}\left(\frac{\partial u}{\partial r}\right)^2. \end{aligned} \tag{2.12}$$

The following boundary conditions are provided for the governing Eq.(2.6), Eq.(2.8), and Eq.(2.12):

$$\begin{aligned} &u = U_w + l_1\frac{\partial u}{\partial r}, \quad v = 0, \quad -k\frac{\partial T}{\partial r} = h_f\left(T_w - T\right) + l_2\frac{\partial T}{\partial r}, \\ &D_B\frac{\partial C}{\partial r} + \frac{D_T}{T_\infty}\frac{\partial T}{\partial r} = l_3\frac{\partial C}{\partial r} \quad \text{at} \quad r = R, \\ &u \to U, \quad T \to T_\infty, \quad C \to C_\infty \quad \text{at} \quad r \to \infty. \end{aligned} \tag{2.13}$$

Where, l_1, l_2 and l_3 are the velocity, thermal, and mass slip, respectively, and h_f represents heat transfer. In the absence of slip flow, l_1, l_2 and l_3 become zero.

To transfigure the set of dimensional PDEs provided in Eqs. (2.6), (2.8), and (2.12) along with boundary conditions presented in Eq.(2.13) into a set of dimensionless ODEs as well as boundary conditions, one can use the transformations as:

$$u = \frac{1}{r}\frac{\partial\psi}{\partial r}, \quad v = -\frac{1}{r}\frac{\partial\psi}{\partial z}, \quad \psi = \left(\nu b\right)^{1/2} z^{n+1/2} R f\left(\eta\right), \quad \eta = \frac{r^2 - R^2}{2R}\left(\frac{b}{\nu}\right)^{1/2} z^{n-1/2}, \tag{2.14}$$

$$T = T_\infty + T_w\left(\frac{bz^n}{2\nu}\right)\theta(\eta), \quad C = C_\infty + C_w\left(\frac{bz^n}{2\nu}\right)\phi(\eta). \qquad \text{(cont. 2.14)}$$

Here T_w, and C_w represent the wall temperature and concentration, respectively. Using Eq.(2.14) in Eqs. (2.6), (2.8), (2.12), and (2.13), one can determine the following set of ordinary differential equations (ODEs):

$$(1+2\kappa\eta)f''' + 2\kappa f'' - nf'^2 + \frac{n+1}{2}ff'' + M(1-f') + Gr\theta + Gm\phi + n = 0, \qquad (2.15)$$

$$\begin{aligned}&\frac{1}{Pr}\left(1+\frac{4}{3}Rd\right)\left[(1+2\kappa\eta)\theta'' + 2\kappa\theta'\right] + (1+2\kappa\eta)\left(Nb\theta'\phi' + Nt\theta'^2\right) + \\ &+Ec(1+2\kappa\eta)f''^2 + Q^*\theta - nf'\theta + \frac{n+1}{2}f\theta' = 0,\end{aligned} \qquad (2.16)$$

$$(1+2\kappa\eta)\phi'' + 2\kappa\phi' + \frac{Nt}{Nb}\left[(1+2\kappa\eta)\theta'' + 2\kappa\theta'\right] + Sc\left(\frac{n+1}{2}f\phi' - nf'\phi - K^*\phi\right) = 0. \qquad (2.17)$$

The border criteria:

$$\begin{aligned}&f' = A + \delta_1 f'', \quad (1+\delta_2)\theta' = -Bi(1-\theta),\\ &Nb(1-\delta_3)\phi' + Nt\theta' = 0 \quad \text{at} \quad \eta = 0,\\ &f' \to 1, \quad \theta \to 0, \quad \phi \to 0 \quad \text{at} \quad \eta \to \infty.\end{aligned} \qquad (2.18)$$

Where, Biot number, $Bi = \frac{\kappa R^2 h_f}{kr}$, curvature, $\kappa = \left(\frac{\nu z^{1-n}}{bR^2}\right)^{1/2}$, magnetic field, $M = \frac{\sigma B_0^2}{\rho_f U}$, thermal Grashof number, $Gr = \frac{z\beta_T g(T_w - T_\infty)}{U^2}$, mass Grashof number, $Gm = \frac{z\beta_c^* g(C_w - C_\infty)}{U^2}$, Prandtl number, $\Pr = \frac{\nu}{\alpha_f}$, radiation, $Rd = \frac{4\sigma^* T_\infty^3}{k^* k_f}$, Brownian motion, $Nb = \frac{\tau D_B (C_w - C_\infty)}{\nu}$, thermophoresis, $Nt = \frac{\tau D_T (T_w - T_\infty)}{\nu T_\infty}$, Eckert number, $Ec = \frac{U^2}{C_p(T_w - T_\infty)}$, heat generation, $Q^* = \frac{Q_0 z}{\rho C_p U}$, Schmidt number, $Sc = \frac{\nu}{D_B}$, chemical reaction, $K^* = \frac{Kz}{U}$, stretching ratio, $A = \frac{a}{b}$, velocity slip, $\delta_1 = \frac{l_1}{R\kappa}$, thermal slip, $\delta_2 = \frac{l_2}{k}$, and concentration slip, $\delta_3 = \frac{l_3}{D_B}$.

For the engineering interest, the physical quantities, especially the skin friction coefficient (C_f), Nusselt number (Nu), and Sherwood number (Sh), are expressed:

$$C_f = \frac{\tau_w}{\rho_f U_w^2}, \quad Nu = \frac{zq_w}{k(T_w - T_\infty)} \quad \text{and} \quad Sh = \frac{zq_m}{D_B(C_w - C_\infty)}. \qquad (2.19)$$

Where, τ_w, q_w, and q_m represent the wall shear stress, heat change, and mass flux, respectively. These may be written as:

$$\tau_w = \mu_f \left(\frac{\partial u}{\partial r}\right)_{r=R}, \quad q_w = -k\left(\frac{\partial T}{\partial r}\right)_{r=R} - \frac{4\sigma^*}{3k^*}\left(\frac{\partial T^4}{\partial r}\right)_{r=R}, \quad \text{and} \quad q_m = -D_B\left(\frac{\partial C}{\partial r}\right)_{r=R}. \tag{2.20}$$

Substituting Eqs. (2.14) and (2.20) into Eq.(2.19), one can find the dimensionless form:

$$\sqrt{Re}C_f = f''(0), \ \frac{Nu}{\sqrt{Re}} = -(1+Rd)\theta'(0), \ \text{and} \ \frac{Sh}{\sqrt{Re}} = -\phi'(0) \tag{2.21}$$

where, $Re = \dfrac{U_w z}{\nu}$ is the Reynold's number.

3. Solution procedure

Using the Runge-Kutta 4th order technique and MATLAB software code, the reduced ODEs shown in Eqs. (2.15)-(2.17) with boundary conditions shown in Eq.(2.18) are numerically solved. The following are the first-order ODEs and the presumptive set of new variables:

$$(y_1, y_2, y_3, y_4, y_5, y_6, y_7)^T = (f, f', f'', \theta, \theta', \phi, \phi')^T, \tag{3.1}$$

$$y_3' = \frac{1}{(1+2\kappa\eta)}\left[-2\kappa y_3 + n y_2^2 - \frac{n+1}{2} y_1 y_3 - M(1-y_2) - Gr y_4 - Gm y_6 - n\right], \tag{3.2}$$

$$\begin{aligned} y_5' = & -\frac{\Pr}{(1+2\kappa\eta)}\left(1+\frac{4}{3}Rd\right)^{-1}\left[\frac{n+1}{2} y_1 y_5 - n y_2 y_4 + Q^* y_4\right] + \\ & -\Pr\left(1+\frac{4}{3}Rd\right)^{-1}\left[(Nb y_5 y_7 + Nt y_5^2) + Ec y_3^2\right] - \frac{1}{(1+2\kappa\eta)} 2\kappa y_5, \end{aligned} \tag{3.3}$$

$$\begin{aligned} y_7' = & -\frac{1}{(1+2\kappa\eta)}\left[2\kappa y_7 + Sc\left(\frac{n+1}{2} y_1 y_7 - n y_2 y_6 - K^* y_6\right) + \right. \\ & -\frac{\Pr^* Nt}{Nb}\left(1+\frac{4}{3}Rd\right)^{-1}\left\{\left(\frac{n+1}{2} y_1 y_5 - n y_2 y_4 + Q^* y_4\right) + \right. \\ & \left.\left. +(1+2\kappa\eta)\left[\left(Nb y_5 y_7 + Nt y_5^2\right) + Ec y_3^2\right]\right\}\right] \end{aligned} \tag{3.4}$$

with boundary conditions

$$y_1 = 0, \quad y_2 = A + \delta_1 y_3, \quad y_4 = 0, \quad (1+\delta_2) y_5 = -Bi(1-y_4),$$

$$Nb(1-\delta_3) y_7 + Nt y_5 = 0 \quad \text{at} \quad \eta = 0, \qquad y_2 \to 1, \quad y_4 \to 0, \quad y_6 \to 0 \quad \text{at} \quad \eta \to \infty.$$

4. Results and discussion

This section presents the variations in fluid velocity, temperature, and concentration distributions under the influence of different controlling factors, such as the magnetic field M $(0.0 \le M \le 9.0)$, slip parameters $(0.0 \le \delta_1 \le 0.3,\ 1.0 \le \delta_2 \le 7.0,\ 0.0 \le \delta_3 \le 0.6)$, curvature $\kappa(0.0 \le 0.6)$, heat generation Q^* $(0.0 \le Q^* \le 0.9)$, Brownian motion Nb $(0.0 \le Nb \le 0.4)$, chemical reaction K^* $(1.0 \le K^* \le 7.0)$, thermophoresis Nt $(0.0 \le Nt \le 0.9)$, radiation Rd $(0.8 \le Rd \le 2.6)$, stretching ratio A $(0.0 \le A \le 1.0)$, power-law index n $(1.0 \le n \le 4.0)$ and Biot number Bi $(0.1 \le Bi \le 0.4)$ through graphical representation as visualized in Figs 2-17. When the impact of one constraint is described, then all others are kept fixed at $M = 1.0,\ n = 1.0,\ Pr = 1.0,\ Gr = 0.3,\ Gm = 0.3,\ Sc = 1.0,\ Rd = 0.01,\ Ec = 0.01,\ Q^* = 1.0,\ K^* = 1.0,\ Bi = 2.0,$ $A = 0.01,\ \delta_1 = 0.01,\ \delta_2 = 0.01,\ \delta_3 = 0.01,\ Nt = 0.2$ and $Nb = 0.2$.

4.1. Magnetic field's impact

Figure 2 elucidates the influences of magnetic field (M) on axial velocity (f'), temperature (θ), and concentration (ϕ) profiles. Figure 2(i) displays that due to increasing magnetic field, the nanofluid's velocity rises in the range $0 \le \eta \le 2.1$ and then static, while $\eta \to \infty$. In contrast, in the range $0 \le \eta \le 3.0$, θ declines for the magnetic field's increasing effect, which is revealed in Fig.2(ii). When the velocity of the free stream is greater than the velocity of stretching, a weak Lorentz force is generated with the larger values of M. The analysis indicates that as the magnetic parameter increases, the free stream velocity dominates the boundary layer and generates a weak Lorentz force. Consequently, the velocity of fluid upsurges and the resistance of the fluid particles decrease, resulting in a decrease in the temperature profile. Figure 2(iii) displays that ϕ upsurges somewhat near the cylindrical surface $(0 \le \eta \le 1.8)$, decreases far away from the surface $(1.8 < \eta \le 3.4)$ within the boundary layer, and then remains unchanged (when $\eta \to \infty$).The temperature gradient causes the fluid to naturally produce viscosity, which is decreased for resistive forces like the drag force, which is produced by the impact of M.

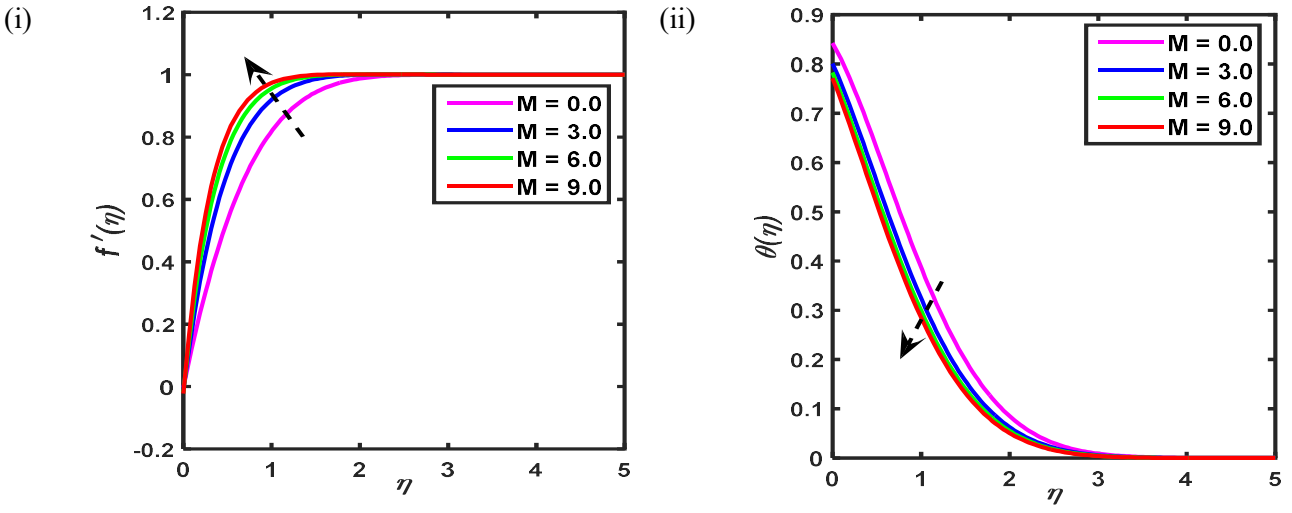

Fig.2. Magnetic field's influence on (i) f' (ii) θ, and (iii) ϕ.

(iii)

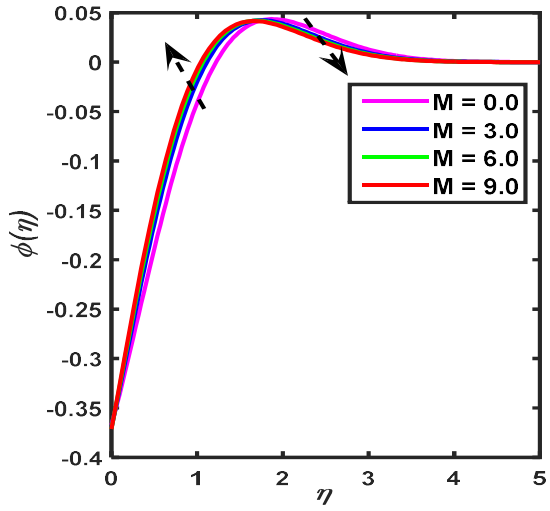

Fig.2 cont. Magnetic field's influence on (i) f' (ii) θ, and (iii) ϕ.

Consequently, as the magnetic induction increases, the fluid's concentration profile increases significantly near the cylindrical surface. Furthermore, Figs 2(i) and 2(ii) show that, in response to the magnetic parameter impacts, the momentum (thermal) boundary layer is expanding (shrinking).

4.2. Influence of curvature (κ)

The effects of curvature on velocity (f'), temperature (θ), and concentration (ϕ) profiles are illustrated in Fig.3. Velocity (slightly), temperature, and concentration profiles lessen in the interval $0 \le \eta \le 2.7$, $0 \le \eta \le 3.1$, and $0 \le \eta \le 3.4$, respectively, for the effects of curvature parameter, and then static at $\eta \to \infty$ which interpreted in Figs 3(i-iii), respectively. From a physical viewpoint of the curvature parameter, it is observed that for an increase in curvature parameter the velocity of fluid declines due to the inverse relationship between a fluid's curvature and speed. Consequently, the fluid velocity, temperature, and concentration of nanoparticles diminish within the BL region, which is noteworthy.

(i)

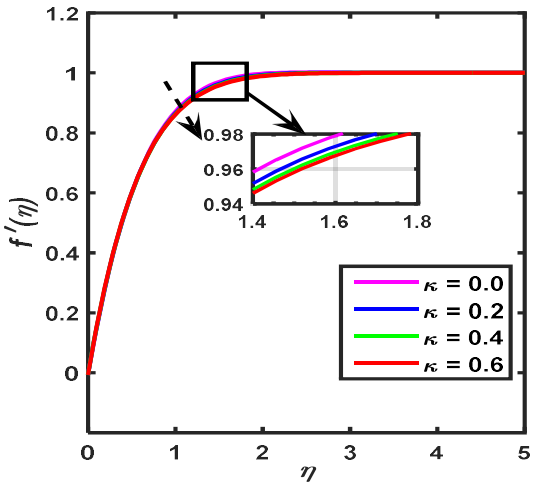

(ii)

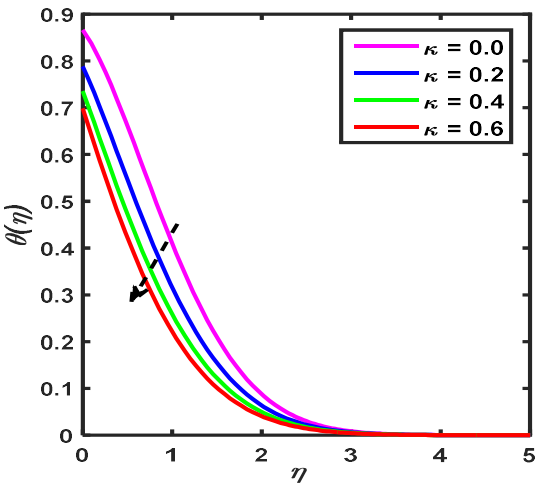

Fig.3. Curvature's effect on (i) f' (ii) θ, and (iii) ϕ.

(iii)

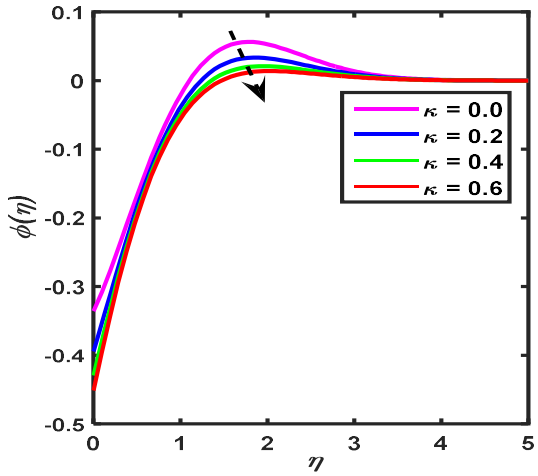

Fig.3 cont. Curvature's effect on (i) f' (ii) θ, and (iii) ϕ.

4.3. Influence of Brownian motion (*Nb*)

Figure 4 designates the consequences of the *Nb* on θ, and ϕ profiles. Figure 4(i) displays that θ and the thickness of thermal BL diminishes slightly in the interval $1.34 \le \eta \le 1.36$ for higher effects of *Nb*. Furthermore, ϕ and thickness of concentration BL increases close to the cylindrical surface $(0 \le \eta \le 1.2)$ as well as decrease distant from the cylindrical surface $(1.2 < \eta \le 3.7)$ and then static $\eta \to \infty$ which is depicted in Fig.4(ii). When fast-moving fluid molecules collide with suspended particles in the fluid, the resultant random or "indecisive" movement of the particles is known as Brownian motion. Viscosity forces in the fluid impede the particle's movement. Particle motion is enhanced by increasing *Nb*. As a result, the temperature profile decreases (slightly), and the concentration profile rises close to the surface and decreases far away from the surface.

(i)

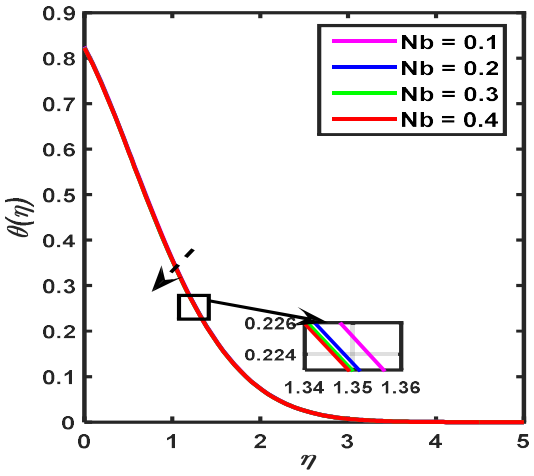

(ii)

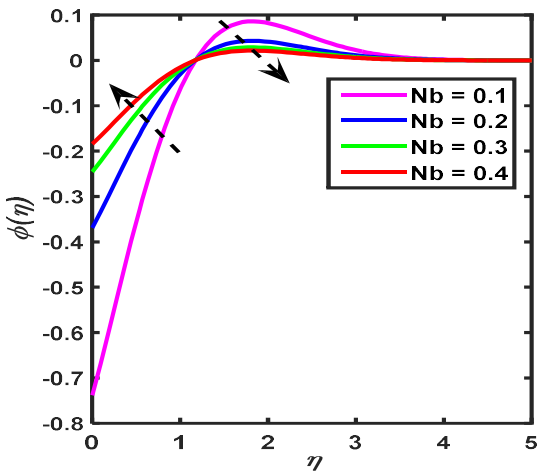

Fig.4. Brownian motion's impact on (i) θ, and (ii) ϕ.

4.4. Influence of thermophoresis (*Nt*)

Figure 5 describes the consequences of *Nt* on f', θ, and ϕ profiles. Figure 5(i-ii) shows that f', and θ decrease in the interval $0.0 \le \eta \le 2.2$, and $0.0 \le \eta \le 3.5$, respectively, as well as the static at $\eta \to \infty$.

However, in Fig.5(iii), if ϕ declines close to the cylindrical surface $(0 \le \eta \le 1.6)$ and surges distant from the surface $(1.6 < \eta \le 3.5)$ then *Nt* does not affect the concentration profile. This fact stems from the physics of thermophoretic force, which is produced near the stretching surface by the temperature difference. This force causes a very low-speed flow for a lower temperature gradient. This means the fluid is heated less and moved near the stretched sheet. Consequently, the temperature and thickness of the BL containing the concentration of nanoparticles decrease as *Nt* grows.

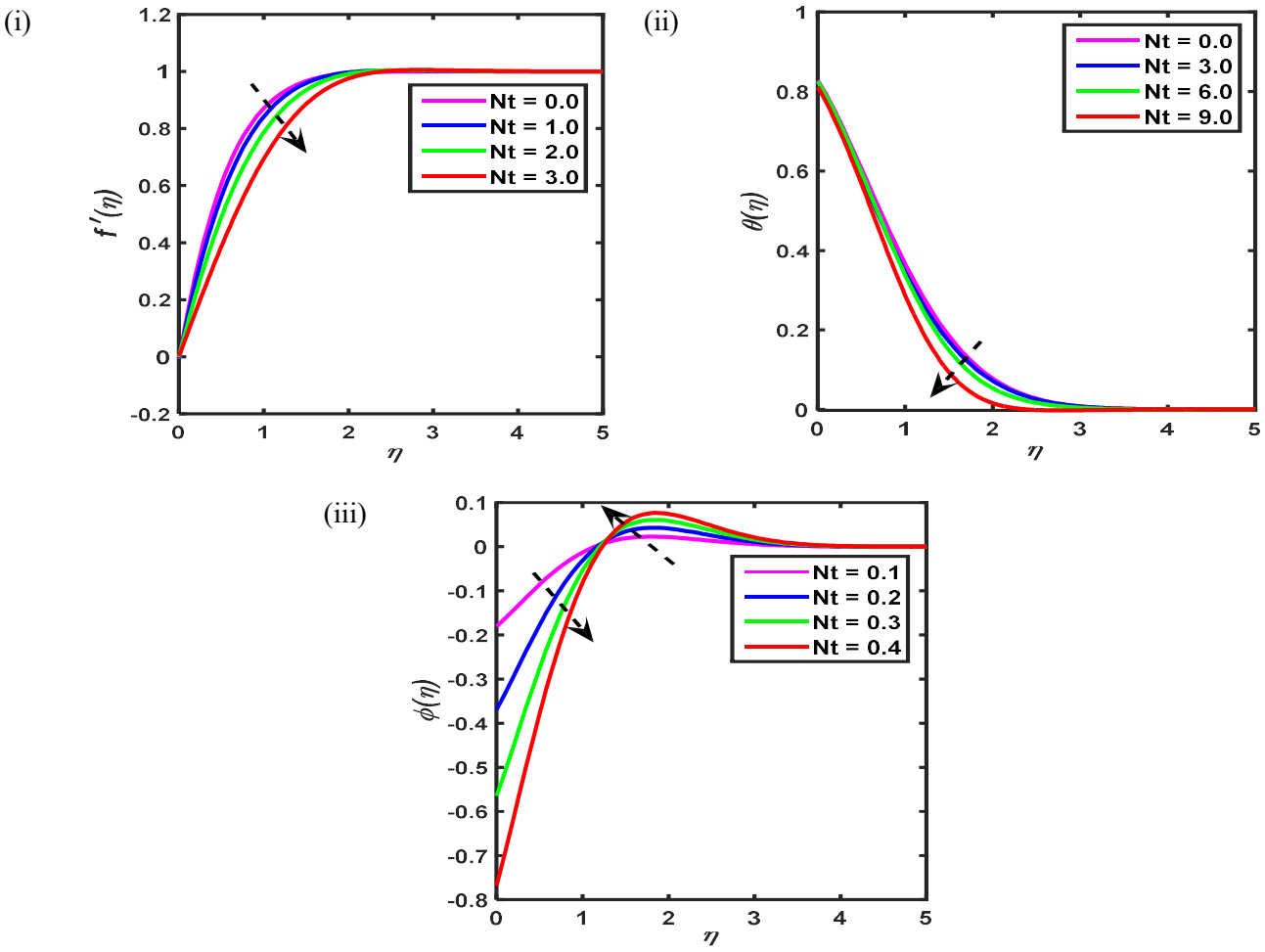

Fig.5. Thermophoresis's influence on (i) f' (ii) θ, and (iii) ϕ.

4.5 Influence of heat generation (Q^*)

Figure 6 illustrates the effects of heat generation parameters on temperature (θ), and concentration (ϕ) profiles. In Fig.6(i) the temperature is enhanced in the interval $0.0 \le \eta \le 3.1$ for larger values of Q^*. However, ϕ diminishes near the cylindrical surface $(0.0 \le \eta \le 1.4)$ and enhances distance from the surface $(1.4 < \eta \le 3.4)$ and then the static $(\eta \to \infty)$ which is elucidated in Fig.6(ii). Heat is generated for positive values of the heat generation parameter; otherwise, heat is absorbed. Physically, a heat absorption coefficient causes the fluid's temperature to decrease. This is so because heat creation in a fluid transforms energy from other sources into thermal energy. Heat generation may raise the temperature and the thermal BL thickness.

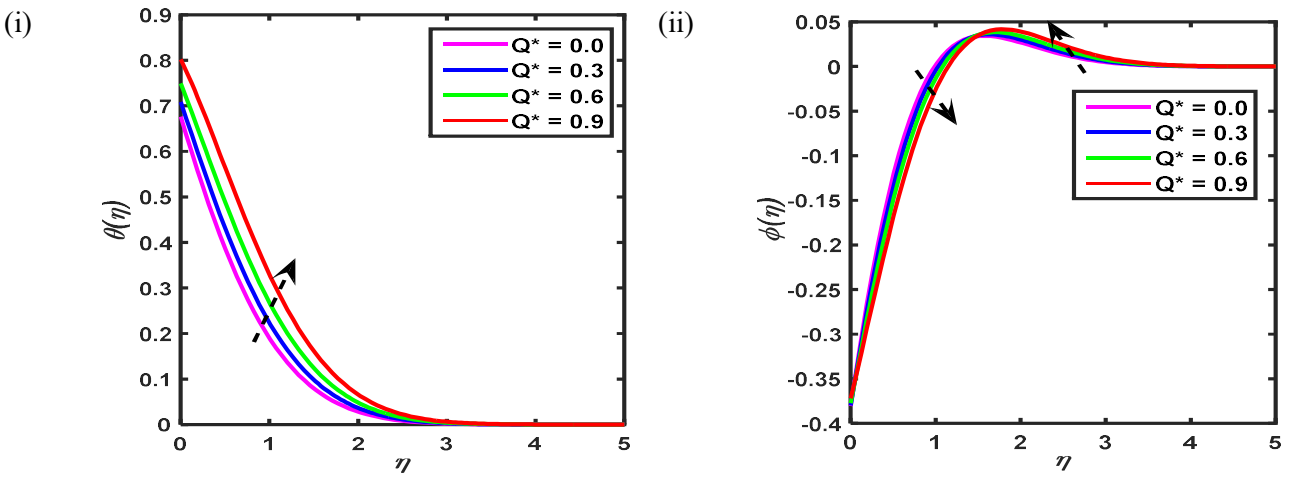

Fig.6. Heat generation's role on (i) θ, and (ii) ϕ.

4.6. Influence of chemical reaction (K^*)

The effects of chemical reaction parameter on ϕ profile is portrayed in Fig.7 ϕ upsurges near the cylindrical surface in the domain $0.0 \le \eta \le 1.2$ and decreases distance from the surface in the domain $1.2 < \eta \le 3.3$ then becomes static at $\eta \to \infty$. From the physics behind chemical reactions, less diffusivity occurs in the flow field, which diminishes the temperature on the surface for higher values of chemical reaction parameters. However, less diffusivity implies more interaction in species concentration. In manufacturing, medicine, etc., chemical reactions have a significant use.

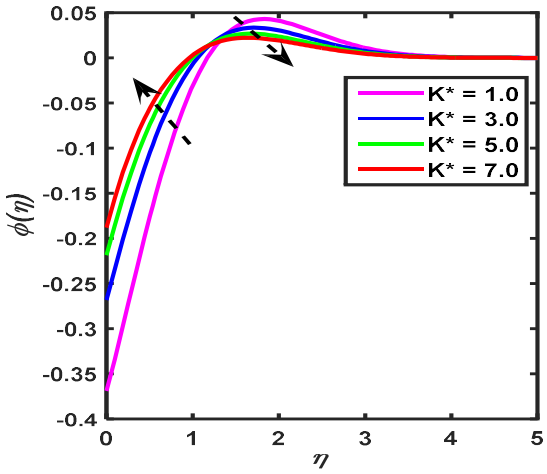

Fig.7. Impact of chemical reaction (K^*) on ϕ.

4.7. Influence of radiation (Rd)

The effects of Rd on temperature (θ), and concentration (ϕ) profiles are designated in Fig.8. In Fig.8(i), θ as well as thermal BL thickness enhance in the domain $0 \le \eta \le 4.9$ for different values of radiation parameter. However, Fig.8(ii) ϕ rises near the cylindrical surface in the domain $0.0 \le \eta \le 0.8$ and falls distance from the surface in the domain $0.8 < \eta \le 3.1$ then becomes static at $\eta \to \infty$. The explanation for these outcomes is that a

rise in the radiation parameter $Rd = \frac{4\sigma^* T_\infty^3}{k^* k_f}$ for a given k_f and T_∞ corresponds to a fall in the Rosseland radiation absorptivity k^*. Hence, the deviation of radiative heat flux q_r enhances since k^* drops down. As a result, the fluid's temperature rises while the radiative heat transfer rate to the fluid improves.

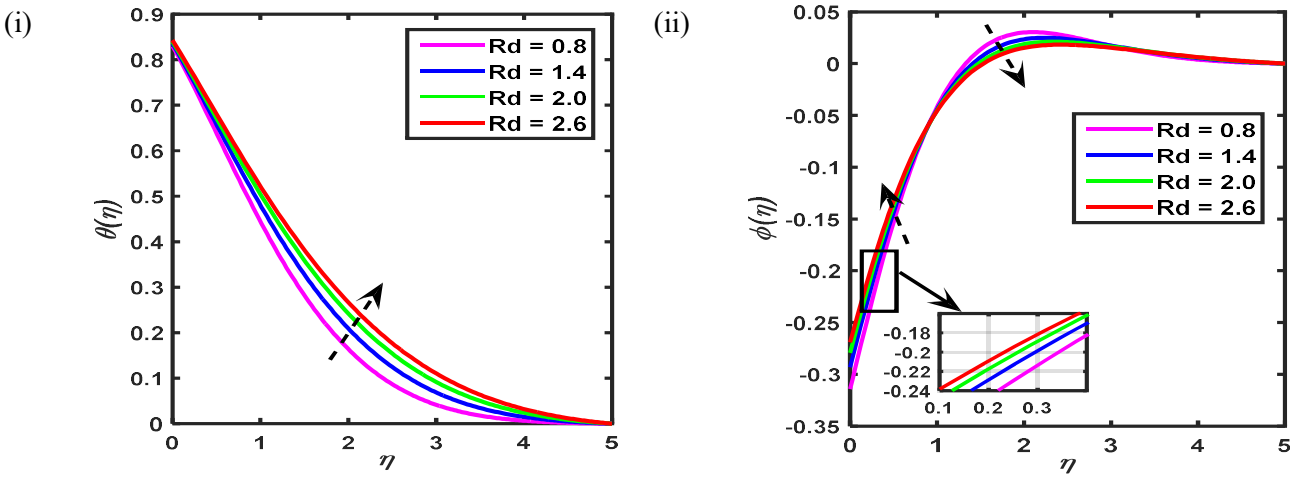

Fig.8. Radiation impact on (i) θ, and (ii) ϕ.

4.8. Influence of stretching ratio (*A*)

Figure 9 highlights the impacts of the stretching ratio on f', θ and ϕ profiles. Figure 9(i) shows that f' and the thickness of the momentum boundary layer rises in the region $0.0 \le \eta \le 2.1$ for increasing values of the stretching ratio parameter. Figure 9(ii) illustrates that θ and thermal BL thickness decreases in the interval $0.0 \le \eta \le 3.0$ for more significant effects of the stretching ratio parameter. However, in Fig.9(iii), ϕ the thickness of the concentration boundary layer upsurges in the vicinity of the cylindrical surface in the interval $0.0 \le \eta \le 1.7$ and decreases far away from the surface in the interval $1.7 < \eta \le 3.2$, and then becomes static at $\eta \to \infty$ for larger values of the stretching parameter.

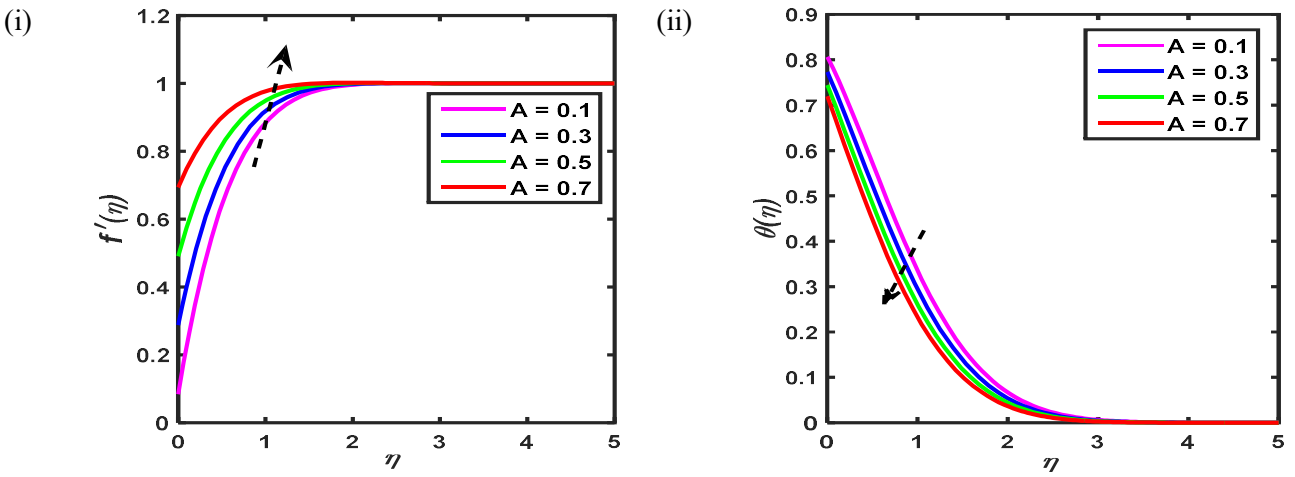

Fig.9. Stretching ratio's influence on (i) f' (ii) θ, and (iii) ϕ.

(iii)

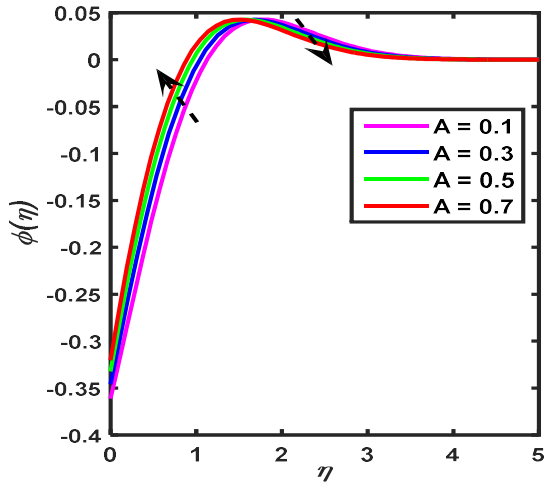

Fig.9 cont. Stretching ratio's influence on (i) f' (ii) θ, and (iii) ϕ.

Physically, increasing the stretching ratio parameter causes the fluid particle's position to change, which enhances the particle's mobility and improves the velocity field. Conversely, a reduction in temperature corresponds to an increase in the stretching parameter.

4.9. Influence of Biot number (*Bi*)

Figure 10 depicts the consequences of Biot number on θ, and ϕ profiles. In Fig.10(i), θ upsurges in the interval $0.0 \le \eta \le 3.1$. However, in Fig.10(ii) the concentration profile decreases near the cylindrical surface in the range $0.0 \le \eta \le 1.0$ and upsurges at a distance from the surface in the interval $1.0 < \eta \le 3.5$ as well as remains static $\eta \to \infty$. From a physical point of view, the relation between internal conductive resistance and convective resistance at an object's surface is shown by the Biot number. Density, temperature, and fluid flow rise with the buoyancy force to enhance thermal energy expandability. The temperature of the cylindrical surface rises with more prominent effects of the Biot number because the strengthening of convection causes the cylindrical surface's heat resistance to decrease.

(i)

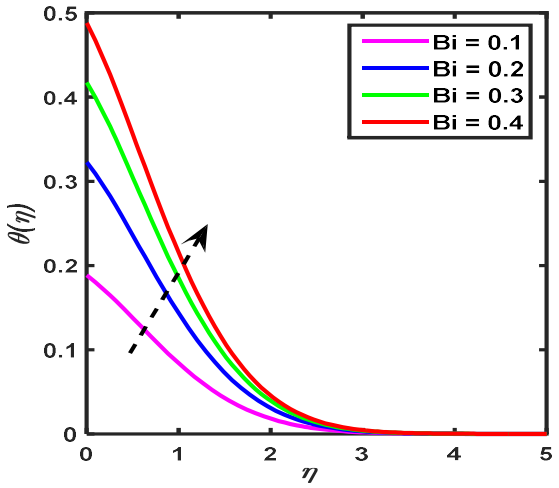

(ii)

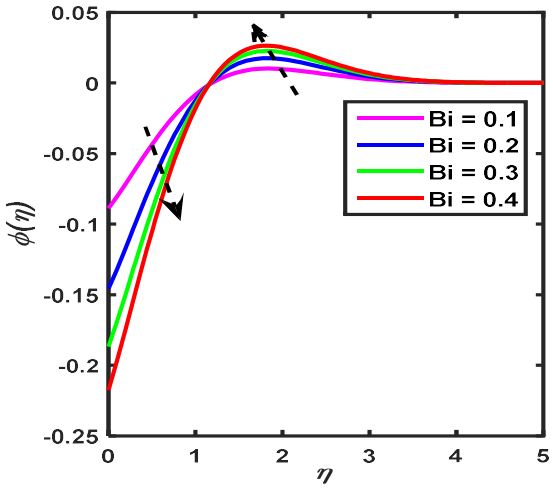

Fig.10. Biot number's role on (i) θ, and (ii) ϕ.

4.10. Influence of Power-law index (*n*)

The consequences of the power-law index on f', θ, and ϕ profiles are depicted in Fig.11. In Fig.11(i), f' and momentum BL thickness rise in the interval $0.0 \le \eta \le 1.8$ for more extensive effects of *n*, and then *n* does not effect on f'. On the other hand, in Fig.11(ii), thermal BL thickness declines in the interval $0.0 \le \eta \le 3.0$ for higher values of n and then static at $\eta \to \infty$. However, in Fig.11(iii) the concentration profile increases near the cylindrical surface in the range $0.0 \le \eta \le 1.1$ and decreases far away from the surface in the interval $1.1 < \eta \le 3.4$ as well as remains static $\eta \to \infty$. It is noted that for $n = 0$ and $n = 1$ the stretched velocity is constant and linear, respectively. On the other hand, for any value of $n > 1$ the stretched velocity is nonlinear. From the relation $U_w = az^n$, it is perceived that for larger effects of *n*, the nonlinearity of the stretched velocity enhances as well as, equivalently, increases the velocity. However, an opposite trend is observed for θ. Owing to the stretched surface, the concentration comes very close to the distance from the surface; consequently, the boundary layer thickness of concentration is reduced distance from the surface.

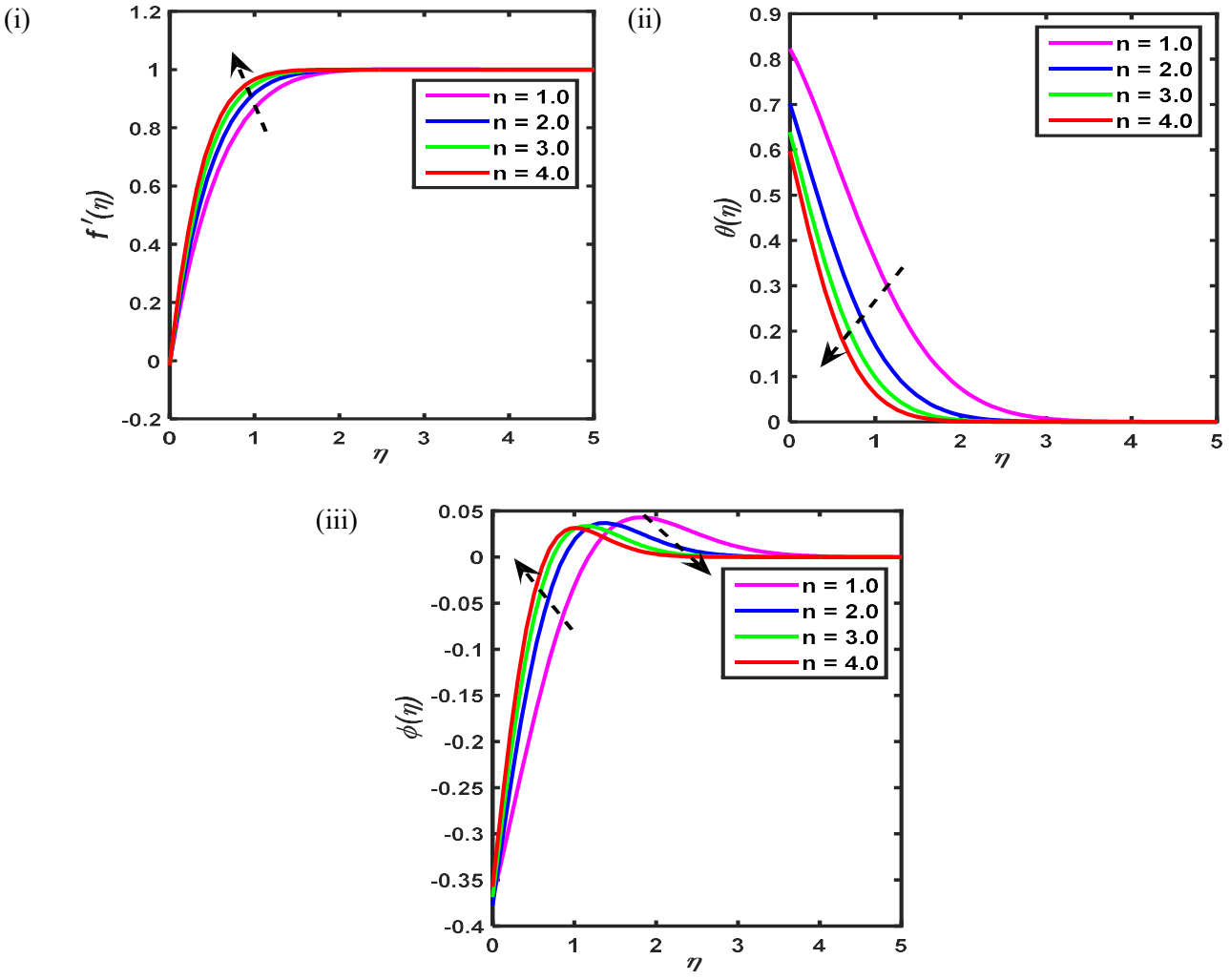

Fig.11. Power-law index's effect on (i) f' (ii) θ, and (iii) ϕ.

4.11. Influence of velocity slip (δ_1)

Figure 12 represents the impacts of the velocity slip parameter on velocity (f'), temperature (θ), and concentration (ϕ) profiles. Figure 12(i) displays that the velocity profile and thickness of momentum BL decline close to the cylindrical surface $0.0 \le \eta \le 2.1$ and then static at $\eta \to \infty$ for larger values of δ_1. On the other hand, θ upsurges in the interval $0.0 \le \eta \le 3.7$ and the thickness of thermal BL increases which is illustrated in Fig.12(ii) for increasing values of the velocity slip parameter However, in Fig.12(iii), ϕ declines close to the cylindrical surface in the domain $0.0 \le \eta \le 1.9$ and increases far away from the surface in the domain $1.9 < \eta \le 4.1$ and then becomes static at $\eta \to \infty$.

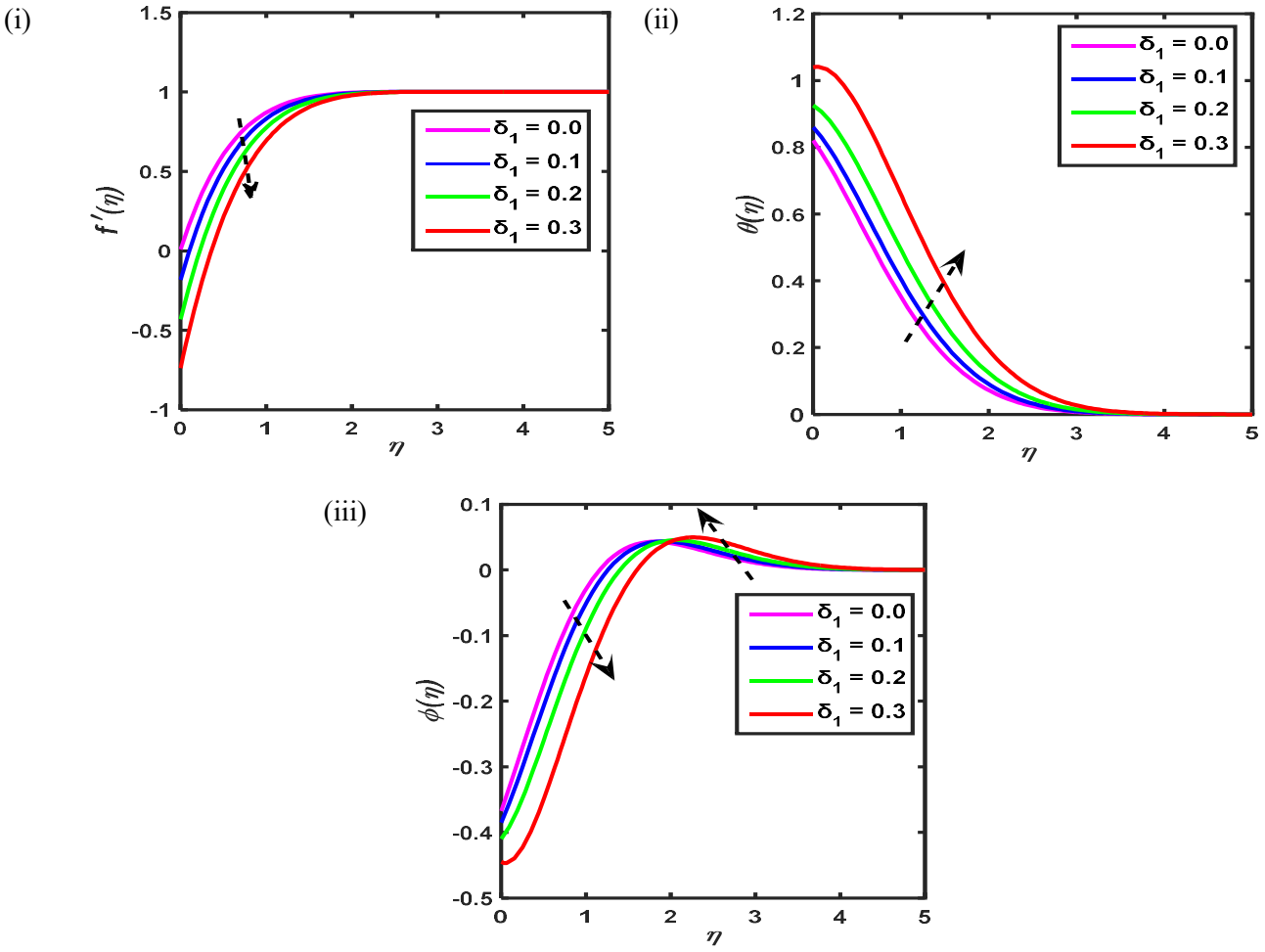

Fig.12. Velocity slip's impact on (i) f' (ii) θ, and (iii) ϕ.

From a physical perspective, it is evident that the velocity of fluid close to the sheet does not stay constant with the rate at which the surface stretches during a slip. Because the slip component, in this case, only results in the stretching surface being partially drawn, it lowers the fluid's speed. In addition, as the slip parameter increases, the thickness of the boundary layer decreases in proximity to the boundary layer. The velocity and concentration of the fluid drop for larger values of δ_1. In the existence of a thermal jump and a magnetic field, fluid temperature rises near the boundary layer as the velocity slip parameter is enhanced.

4.12. Influence of thermal slip (δ_2)

Figure 13 signifies the influences of the thermal slip parameter on θ, and ϕ profiles. In Fig. 13(i), it is detected that θ decreases in the interval $0.0 \le \eta \le 3.0$, then static at $\eta \to \infty$ for higher values of thermal slip parameter. As well as, the thickness of thermal boundary layer declines. However, in Fig.13(ii), the concentration profile increases near the cylindrical surface in the domain $0.0 \le \eta \le 1.1$ and decreases far away from the surface in the domain $1.1 < \eta \le 3.5$ and then becomes static at $\eta \to \infty$. From the physical point of view, the thermal slip parameter can resist the temperature inside the flow. The thermal boundary layer thickness falls as the value of the thermal slip parameter grows, even when a tiny quantity of heat is transported from the surface to the fluid.

(i) (ii)

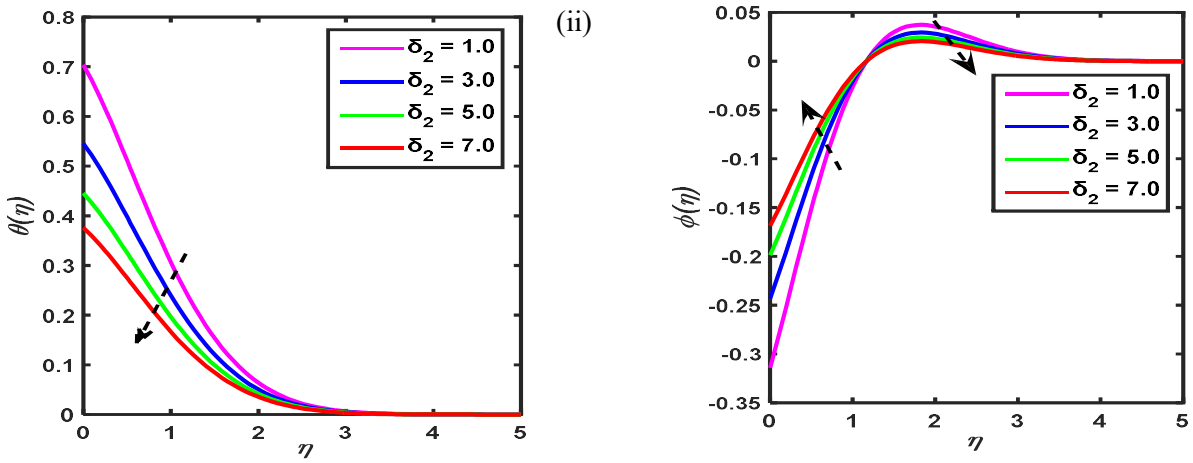

Fig.13. Thermal slip's influence on (i) θ, and (ii) ϕ.

4.13. Influence of concentration slip (δ_3)

Figure 14 depicts the impacts of the concentration slip parameter on ϕ profile. It is detected that ϕ profile decreases in the interval $0.0 \le \eta \le 2.1$, then remains static at $\eta \to \infty$ for higher values of the concentration slip parameter. Slip essentially slows down fluid mobility, which ultimately results in a decrease in net molecular movement. As a result, the mass fraction fields drop with less molecular mobility.

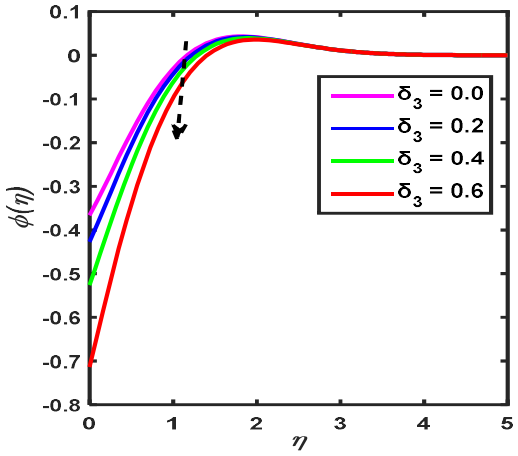

Fig.14. Impact of concentration slip on ϕ.

4.14. Skin friction, thermal, and mass transport

Tables 1 and 2 are erected to present the values of velocity gradient (skin friction), rate of heat transfer (Nusselt number), and rate of mass transfer (Sherwood number) for the impacts of parameters M, n, Nt, Nb, κ, Rd, Bi, Q^*, K^*, A, δ_1, δ_2, δ_3 numerically. From Tabs. 1 and 2, it is perceived that the velocity gradient declines with the increasing impact of the parameters Nt, A, δ_2,δ_3, and upsurges for the parameters M, n, Nt, κ, Rd, Bi, Q^*, K^*, δ_1. From a physical point of view, the fluid exerts a drag force on the cylindrical surface when the skin friction coefficient is positive and vice versa when the skin friction coefficient is negative. On the other hand, the heat transfer rate diminishes the effects of M, n, Nt, κ, Rd, Bi, A, K^*, δ_3, nevertheless raising the mass transfer rate. Alternatively, the thermal transfer rate enhances the effects Rd, Q^*, δ_1,δ_2, but the reverse behaviour occurs when it comes to the mass transfer rate.

Table 1. $f''(0)$, $\theta'(0)$, and $\phi'(0)$ values due to M, n, Nt, Nb, κ variations with $\Pr = 1.0$, $Gr = 0.3$, $Gm = 0.3$, $Sc = 1.0$, $Rd = 0.01$, $Ec = 0.01$, $Q^* = 1.0$, $K^* = 1.0$, $Bi = 2.0$, $A = 0.01$, $\delta_1 = 0.01$, $\delta_2 = 0.01$, $\delta_3 = 0.01$.

M	n	Nb	Nt	κ	$f''(0)$	$-\theta'(0)$	$-\phi'(0)$
0.0	1.0	0.2	0.2	0.1	1.3801	-0.3118	0.3150
3.0					2.1997	-0.3937	0.3977
6.0					2.7946	-0.4302	0.4345
9.0					3.2886	-0.4529	0.4575
1.0	1.0	0.2	0.2	0.1	1.6965	-0.3498	0.3533
	2.0				2.0521	-0.5905	0.5964
	3.0				2.3636	-0.7139	0.7211
	4.0				2.6410	-0.7971	0.8051
1.0	1.0	0.1	0.2	0.1	1.6631	-0.3469	0.7008
		0.2			1.6965	-0.3498	0.3533
		0.3			1.7076	-0.3507	0.2362
		0.4			1.7131	-0.3512	0.1774
1.0	1.0	0.2	0.1	0.1	1.7146	-0.3448	0.1741
			0.2		1.6965	-0.3498	0.3533
			0.3		1.6773	-0.3544	0.5369
			0.4		1.6571	-0.3586	0.7244
1.0	1.0	0.2	0.2	0.1	1.6965	-0.3498	0.3533
					2.0286	-0.3940	0.3980
					2.3274	-0.4277	0.4321
					2.6031	-0.4551	0.4597
1.0	1.0	0.2	0.2	0.1	1.6965	-0.3498	0.3533
					1.3480	-0.3170	0.3202
					0.9554	-0.2708	0.2736
					0.4712	-0.1897	0.1916
1.0	1.0	0.2	0.2	0.0	1.6831	-0.2652	0.2678
				0.2	1.7099	-0.4188	0.4230
				0.4	1.7356	-0.5230	0.5283
				0.6	1.7590	-0.5971	0.6031

Table 2. The scheming table for $f''(0)$, $\theta'(0)$, and $\phi'(0)$, with diverse values of Rd, Bi, Q^*, K^*, A, δ_1, δ_2, δ_3 with fixed $M = 1.0$, $n = 1.0$, $Pr = 1.0$, $Gr = 0.3$, $Nb = 0.2$, $Nt = 0.2$, $Gr = 0.3$, $Gm = 0.3$, $\kappa = 1.0$, $Sc = 1.0$, $Ec = 0.01$.

Rd	Bi	K^*	Q^*	A	δ_1	δ_2	δ_3	$f''(0)$	$-\theta'(0)$	$-\phi'(0)$
0.8	2.0	1.0	1.0	0.01	0.01	0.01	0.01	1.7103	-0.3373	0.3407
1.4								1.7164	-0.3261	0.3293
2.0								1.7207	-0.3172	0.3204
2.6								1.7239	-0.3102	0.3134
0.01	2.0	1.0	1.0	0.01	0.01	0.01	0.01	1.6981	-0.3437	0.3471
2.5								1.6182	-0.6396	0.6460
3.0								1.5423	-0.9148	0.9240
3.5								1.4707	-1.1700	1.1818
0.01	0.1	1.0	1.0	0.01	0.01	0.01	0.01	1.6386	-0.0804	0.0812
	0.2							1.6513	-0.1341	0.1355
	0.3							1.6601	-0.1731	0.1748
	0.4							1.6666	-0.2028	0.2048
0.01	2.0	1.0	1.0	0.01	0.01	0.01	0.01	1.6965	-0.3498	0.3533
		3.0						1.7075	-0.3568	0.3604
		5.0						1.7125	-0.3603	0.3640
		7.0						1.7153	-0.3625	0.3662
0.01	2.0	1.0	0.0	0.01	0.01	0.01	0.01	1.6685	-0.6409	0.6474
			0.3					1.6743	-0.5762	0.5821
			0.6					1.6819	-0.4959	0.5010
			0.9					1.6922	-0.3920	0.3959
0.01	2.0	1.0	1.0	0.1	0.01	0.01	0.01	1.5718	-0.3833	0.3872
				0.3				1.2760	-0.4494	0.4539
				0.5				0.9554	-0.5062	0.5113
				0.7				0.6112	-0.5557	0.5613
0.01	2.0	1.0	1.0	0.01	0.0	0.01	0.01	1.6737	-0.3562	0.3598
					0.1			1.9208	-0.2769	0.2797
					0.2			2.2040	-0.1478	0.1493
					0.3			2.4931	0.0777	-0.0785
0.01	2.0	1.0	1.0	0.01	0.01	1.0	0.01	1.6860	-0.2962	0.2992
						3.0		1.6718	-0.2273	0.2296
						5.0		1.6627	-0.1849	0.1867
						7.0		1.6563	-0.1560	0.1576
0.01	2.0	1.0	1.0	0.01	0.01	0.01	0.0	1.6967	-0.3499	0.3499
							0.2	1.6913	-0.3459	0.4323
							0.4	1.6825	-0.3393	0.5655
							0.6	1.6659	-0.3269	0.8172

5. Multiple regression analysis

In Tab.3, $R^2 = 0.9966$ is obtained, which means that the mentioned parameters cause a *99.66%* change in skin friction. The *p*-value is chosen as *0.05*. Consequently, a significant relationship exists between the parameters mentioned and the skin friction coefficient. The regression model is:

$$f''(0) = 1.07 + 0.208M + 0.323n + 0.132Nb - 0.191Nt + 0.129\kappa + 0.012Rd + \\ +0.024Bi + 0.004K^* + 0.029Q^* - 1.539A + 2.713\delta_1 - 0.006\delta_2 - 0.044\delta_3. \tag{5.1}$$

It is clarified that changing one unit in the parameters mentioned will change the skin friction coefficient. Here, the coefficient of *M* is *0.208*; a one-unit change in the magnetic parameter will result in a *0.208*-unit change in the skin friction coefficient. It is seen that the coefficient is positive, which designates a positive relationship between *M* and the skin friction coefficient. Additionally, it is seen that when *M* increases by one unit, then the skin friction coefficient will also increase by *0.208* units. Similarly, the remaining parameters can be interpreted on the skin friction coefficient.

Table 3. The multiple regression analysis of skin friction coefficient $\left(f''\ (0)\right)$.

SUMMARY OUTPUT OF LOCAL SKIN FRICTION COEFFICIENT $\left(f''\ (0)\right)$						
Regression Statistics						
Multiple *R*	R^2	Adjusted R^2	Standard error	Observations		
0.998	*0.996*	*0.9946*	*0.0295*	*52*		
ANOVA						
	df	*SS*	*MS*	*F*	Significance *F*	
Regression	*13*	*8.139848*	*0.626142*	*719.0904*	*2.98E-41*	
Residual	*38*	*0.033088*	*0.000871*			
Total	*51*	*8.172936*				
	Coefficients	Standard Error	*t* -stat	*p*-value	Lower *95%*	Upper *95%*
Intercept	*1.07093392*	*0.04606147*	*23.2501017*	*4.51179E-24*	*0.977687346*	*1.1641805*
M	*0.20810334*	*0.00319604*	*65.1129412*	*1.36124E-40*	*0.201633298*	*0.21457337*
n	*0.32344837*	*0.00837102*	*38.639047*	*4.12917E-32*	*0.306502123*	*0.34039463*
Nb	*0.13226514*	*0.12242936*	*1.08033838*	*0.28680069*	*-0.11558014*	*0.38011041*
Nt	*-0.19073487*	*0.12242936*	*-1.5579177*	*0.1275432*	*-0.43858014*	*0.05711041*
κ	*0.12867676*	*0.05128881*	*2.50886628*	*0.01649616*	*0.024847997*	*0.23250552*
Rd	*0.01234799*	*0.00877789*	*1.40671402*	*0.16763838*	*-0.00542193*	*0.0301179*
Bi	*0.02400677*	*0.0092024*	*2.6087523*	*0.01292256*	*0.005377494*	*0.04263604*
K^*	*0.00372776*	*0.00418551*	*0.89063389*	*0.37873009*	*-0.00474537*	*0.01220088*
Q^*	*0.02890663*	*0.02449246*	*1.18022597*	*0.24524585*	*-0.02067575*	*0.07848902*
A	*-1.53868124*	*0.03516879*	*-43.751325*	*4.06689E-34*	*-1.60987674*	*-1.4674857*
δ_1	*2.71276124*	*0.08716283*	*31.1229153*	*1.19794E-28*	*2.536309321*	*2.88921315*
δ_2	*-0.00622211*	*0.00345917*	*-1.7987308*	*0.08000793*	*-0.01322482*	*0.00078061*
δ_3	*-0.04388839*	*0.04270716*	*-1.0276589*	*0.31060757*	*-0.13034451*	*0.04256773*

From Tab.3, it is clear that the p-values of the variables *Nb*, *Nt*, *Rd*, K^*, Q^*, δ_2, and δ_3 are higher than the considered value of *0.05*. Thus, we can say that these variables are insignificant for the regression Eq.(5.1). So, the final regression model for the skin friction coefficient of multiple independent variables becomes:

$$f''(0) = 1.07 + 0.208\,\mathrm{M} + 0.323\,\mathrm{n} + 0.129\kappa + 0.024\,\mathrm{Bi} - 1.539A + 2.713\delta_1. \tag{5.2}$$

Table 4 shows that the multiple *R*-value is *0.9894*, which means that the mentioned parameters cause a *98.94*% change in the Nusselt number. Consequently, a significant relationship exists between the parameters mentioned and the Nusselt number, and the *p*-value is *0.05*. The regression model is:

$$\begin{aligned}\theta'(0) = {} & -0.193 - 0.014M - 0.163n + 0.002Nb - 0.032Nt - 0.522\kappa + 0.018Rd - \\ & + 0.119Bi - 0.002K^* + 0.303Q^* - 0.303A + 1.333\delta_1 + 0.032\delta_2 + 0.043\delta_3.\end{aligned} \tag{5.3}$$

It is illuminated that changing one unit in the parameters mentioned will change the Nusselt number. Here, the coefficient of *Nt* is *-0.032*, a one-unit change in the thermophoresis parameter will result in a *0.032* unit change in the Nusselt number. It is observed that the coefficient is negative, which designates the negative relationship between *Nt* and the Nusselt number. Additionally, it is noticed that when *Nt* decreases by one unit, then the Nusselt number will also decrease by *0.032* units. Similarly, the remaining parameters can be interpreted using the Nusselt number.

From Tab.4, it is clear that the *p*-values of the variables *Nb*, *Nt*, K^*, Q^*, and δ_3 are higher than the considered value *0.05*. Thus, we can say that these variables are insignificant for the regression Eq.(5.3). So, the final regression model for the heat transport rate is:

$$\begin{aligned}\theta'(0) = {} & -0.193 - 0.014M - 0.163n - 0.522\kappa + 0.018Rd - \\ & + 0.119Bi - 0.303A + 1.333\delta_1 + 0.032\delta_2.\end{aligned} \tag{5.4}$$

Table 4. The multiple regression analysis of Nusselt number $\left(-\theta'(0)\right)$.

SUMMARY OUTPUT of $\left(-\theta'(0)\right)$						
Regression Statistics						
Multiple *R*	*R*^{2}		Adjusted *R*^{2}	Standard error	Observations	
0.989426	*0.978964*		*0.971768*	*0.02609*	*52*	
ANOVA						
	df	*SS*	*MS*	*F*	Significance *F*	
Regression	*13*	*1.2037755*	*0.092598*	*136.034918*	*1.0793E-27*	
Residual	*38*	*0.0258664*	*0.000681*			
Total	*51*	*1.2296419*				
	Coefficients	Standard error	*t* stat	*p*-value	Lower 95%	Upper 95%
Intercept	*-0.19346*	*0.0407257*	*-4.750298*	*2.8872E-05*	*-0.2759043*	*-0.1110144*
M	*-0.01381*	*0.0028258*	*-4.887912*	*1.8831E-05*	*-0.0195329*	*-0.0080918*
n	*-0.1634*	*0.0074013*	*-22.07666*	*2.8285E-23*	*-0.1783798*	*-0.1484134*
Nb	*0.001915*	*0.1082472*	*0.0176912*	*0.98597776*	*-0.21722*	*0.22105004*
Nt	*-0.03242*	*0.1082472*	*-0.299484*	*0.76620276*	*-0.2515533*	*0.18671671*

Table 4 cont. The multiple regression analysis of Nusselt number $\left(-\theta'\ (0)\right)$.

SUMMARY OUTPUT of $\left(-\theta'\ (0)\right)$						
Regression Statistics						
Multiple *R*	R^2		Adjusted R^2	Standard error	Observations	
0.989426	*0.978964*		*0.971768*	*0.02609*	*52*	
ANOVA						
	df	*SS*	*MS*	*F*	Significance *F*	
Regression	*13*	*1.2037755*	*0.092598*	*136.034918*	*1.0793E-27*	
Residual	*38*	*0.0258664*	*0.000681*			
Total	*51*	*1.2296419*				
	Coefficients	Standard error	*t* stat	*p*-value	Lower 95%	Upper 95%
Intercept	*-0.19346*	*0.0407257*	*-4.750298*	*2.8872E-05*	*-0.2759043*	*-0.1110144*
κ	*-0.52186*	*0.0453475*	*-11.50806*	*5.9862E-14*	*-0.6136635*	*-0.4300609*
Rd	*0.01788*	*0.0077611*	*2.3037622*	*0.02679876*	*0.00216819*	*0.03359111*
Bi	*-0.11893*	*0.0081364*	*-14.61697*	*3.4945E-17*	*-0.1354007*	*-0.1024581*
K^*	*-0.00153*	*0.0037007*	*-0.413564*	*0.68151798*	*-0.0090221*	*0.00596114*
Q^*	*0.303443*	*0.0216553*	*14.012456*	*1.3615E-16*	*0.25960463*	*0.34728221*
A	*-0.30253*	*0.0310949*	*-9.729123*	*7.283E-12*	*-0.3654739*	*-0.2395774*
δ_1	*1.332942*	*0.0770659*	*17.296122*	*1.321E-19*	*1.17692995*	*1.4889536*
δ_2	*0.031772*	*0.0030585*	*10.388223*	*1.172E-12*	*0.02558042*	*0.03796347*
δ_3	*0.042585*	*0.03776*	*1.127773*	*0.26648642*	*-0.0338564*	*0.11902578*

Table 5 shows that the multiple *R*-value is *0.9768*, indicating that the mentioned parameters account for a *97.68*% change in the Sherwood number. Consequently, a significant relationship exists between the parameters mentioned and the Sherwood number. The regression model is:

$$\begin{aligned}\phi'(0) &= 0.117 + 0.012M + 0.159n - 1.42Nb + 1.782Nt + 0.496\kappa - 0.025Rd + \\ &+0.128Bi - 0.001K^* - 0.288Q^* - 0.279A - 1.407\delta_1 - 0.035\delta_2 + 0.654\delta_3.\end{aligned} \tag{5.5}$$

It is illuminated that changing one unit in the parameters mentioned will change the Sherwood number. Here, the coefficient of κ is *0.496*; a one-unit change in the curvature parameter will result in a 0.496-unit change in the Sherwood number. It is observed that the coefficient is positive, which designates the positive relationship between the curvature parameter and the Sherwood number. Additionally, it is noticed that when κ increases by one unit, then the Sherwood number will increase by *0.496* units. Similarly, the remaining parameters can be interpreted on the Sherwood number.

From Tab.5, it is clear that the p-value of the variables *Rd*, and K^* are higher than *0.05*. Thus, we can say that these variables are insignificant for the regression Eq.(5.5). So, the final regression model for the rate of material transfer is as:

$$\begin{aligned}\phi'(0) &= 0.117 + 0.012M + 0.159n - 1.42Nb + 1.782Nt + 0.496\kappa + \\ &+0.128Bi - 0.288Q^* - 0.279A - 1.407\delta_1 - 0.035\delta_2 + 0.654\delta_3.\end{aligned} \tag{5.6}$$

Table 5. The multiple regression analysis of Sherwood number $\left(-\phi'(0)\right)$.

SUMMARY OUTPUT of $\left(-\phi'(0)\right)$						
Regression Statistics						
Multiple *R*	R^2	Adjusted R^2		Standard error	Observations	
0.9768	*0.9542*	*0.9385*		*0.0469*	*52*	
ANOVA						
	df	*SS*	*MS*	*F*	Significance *F*	
Regression	*13*	*1.744287*	*0.134176*	*60.88518*	*2.5E-21*	
Residual	*38*	*0.083743*	*0.002204*			
Total	*51*	*1.82803*				
	Coefficients	Standard error	*t* stat	*p*-value	Lower 95%	Upper 95%
Intercept	*0.11700976*	*0.07327817*	*1.59678876*	*0.118596619*	*-0.0313341*	*0.26535367*
M	*0.01187804*	*0.00508450*	*2.33612581*	*0.02486044*	*0.00158500*	*0.02217108*
n	*0.15906334*	*0.01331728*	*11.9441352*	*1.96347E-14*	*0.13210392*	*0.18602275*
Nb	*-1.4202296*	*0.19477015*	*-7.2918238*	*9.9418E-09*	*-1.8145211*	*-1.0259380*
Nt	*1.78210375*	*0.19477015*	*9.14977873*	*3.79991E-11*	*1.3878122*	*2.1763953*
κ	*0.49618028*	*0.08159422*	*6.08107118*	*4.40679E-07*	*0.33100141*	*0.66135914*
Rd	*-0.0251747*	*0.01396456*	*-1.8027533*	*0.079362139*	*-0.0534444*	*0.00309512*
Bi	*0.12806196*	*0.01463988*	*8.74747131*	*1.2268E-10*	*0.09842507*	*0.15769886*
K^*	*-0.0014291*	*0.00665864*	*-0.2146152*	*0.83121493*	*-0.0149088*	*0.01205066*
Q^*	*-0.2881256*	*0.03896451*	*-7.3945656*	*7.2394E-09*	*-0.3670051*	*-0.2092461*
A	*0.27868574*	*0.05594925*	*4.98104521*	*1.4086E-05*	*0.16542241*	*0.39194908*
δ_1	*-1.4071462*	*0.13866540*	*-10.147781*	*2.26734E-12*	*-1.6878596*	*-1.1264328*
δ_2	*-0.0347499*	*0.00550311*	*-6.3145942*	*2.10932E-07*	*-0.0458904*	*-0.0236094*
δ_3	*0.65394315*	*0.06794187*	*9.6250395*	*9.7686E-12*	*0.51640203*	*0.79148426*

Table 6. Comparison the numerical value of skin friction coefficient $\left(f''(0)\right)$ with the earlier works of Abdel-Wahed and El-Said [51], and Nadeem *et al.* [52] for $n = 1,\ Nb = Nt = 0.1,\ Bi = 0.5,\ \ A = 1.0,\ \delta_1 = \delta_2 = \delta_3 = 0.0,\ \mathrm{Pr} = 7.0,\ Sc = 2.0$.

Parameters	Present works	Abdel-Wahed and El-Said [51]	Nadeem *et al.* [52]
$M = 0,\ \kappa = 0$	*-1.0014*	*-1.0048*	*-1.0042*

To verify the accuracy of the obtained results, a comparison is provided in Table 6 between the present findings and those of Abdel-Wahed and El-Said [51] and Nadeem et al. [52]. It is observed that the computed results show good agreement with the published results.

6. Conclusion

This article investigates the hydromagnetic nanofluid's BL flow under multiple slip conditions and surface curvature. The imitation of the magnetic field effect with radiation, viscous dissipation, and chemical reaction is also incorporated. The notable detection of the above analysis is outlined as follows:

- The skin friction coefficient increases by *58%, 56%*, and *49%* due to the increasing values of the magnetic parameter, power-law index parameter, and velocity slip, respectively. Conversely, the skin friction declines by approximately *61%* for the escalating stretching ratio.
- The Nusselt number increases by about *39%, 78%,* and *47%* for the rising values of the heat generation, velocity slip, and thermal slip, respectively. However, the heat transport rate decreases by approximately *45%, 56%, 56%, 45%, 60%,* and *69%* due to increasing magnetic induction, power-law index, curvature, stretching ratio, Biot number, and chemical reaction, respectively.
- The rising values of the magnetic field, power-law index, thermophoresis, curvature, Biot number, stretching ratio, and concentration slip increase the rate of mass transport by about *45%, 56%, 76%, 56%, 60%, 45%,* and *57%*, respectively. The Sherwood number decreases about *75%, 39%, 78%,* and *47%* for growing values of Brownian motion, heat generation, velocity slip, and thermal slip, respectively.
- The magnetic field, stretching ratio, and power-law index act as controlling parameters because the fluid velocity and the heat transfer rate enhance within the BL region but the rate of mass transfer declines.
- The effect of magnetic induction, stretching ratio, power-law index, velocity slip, thermal slip, Brownian motion, thermophoresis, heat generation, radiation, Biot number, and chemical reaction act as an oscillatory response toward concentration profile.
- The magnetic strength, velocity slip, power-law index, and stretching ratio are statistically significant with skin friction coefficients.
- The magnetic field, stretching ratio, curvature, power-law index, velocity slip, thermal slip, thermophoresis, heat generation, radiation, and Biot number are statistically significant with the Nusselt number.

The current model assumes steady, laminar flow with constant thermophysical properties and neglects nanoparticle interactions such as agglomeration, Brownian motion effects beyond first order, and turbulence. It also considers a single type of nanoparticle and a specific cylindrical geometry. Future work could extend the model to unsteady or three-dimensional flows, incorporate variable properties and non-Newtonian nanofluids, explore different particle types or hybrid nanofluids, and include experimental validation. Additionally, the effects of turbulence, more complex chemical reactions, and advanced slip models could be investigated to enhance the applicability of the results to industrial and biomedical systems.

Data availability

There is no data and material to be available.

Funding declaration

The authors declare that no funds or grants were taken during the preparation of this manuscript.

Contributions

A. Umme Hani wrote the manuscript and prepared the Figs 1-8, B. Mohammad Ali wrote the manuscript and prepared the Figs. 9-14, C.R. Nasrin supervised and edited the manuscript. All authors reviewed the manuscript.

Competing interests

The authors declare that they have no competing interests in this study.

Nomenclature

a – stretching constant
a – stretching ratio
b – free stream rate constant
B_0 – transverse magnetic induction $\left[kgs^{-2}A^{-1}\right]$
Bi – Biot number
C – dimensional concentration $\left[kgm^{-3}\right]$
C_f – skin friction coefficient
C_p – specific heat $\left[Jkg^{-1}K^{-1}\right]$
C_w – wall concentration $\left[kgm^{-3}\right]$
C_∞ – free stream concentration $\left[kgm^{-3}\right]$
D_B – Brownian diffusion $\left[cm^2s^{-1}\right]$
D_T – Thermophoresis diffusion
$f(\eta)$ – dimensionless stream function
$f'(\eta)$ – dimensionless velocity
$f''(\eta)$ – dimensionless velocity gradient
g – gravity $\left[ms^{-2}\right]$
Gm – mass Grashof number
Gr – Grashof number
h_f – coefficient of heat transfer
k – chemical reaction/thermal conductivity $\left[Wm^{-1}K^{-1}\right]$
k^* – chemical reaction
l_1 – velocity slip
l_2 – thermal slip
l_3 – concentration slip
m – magnetic field
n – power-law index
Nb – Brownian motion
Nt – thermophoresis
Nu – Nusselt number
Q_0 – heat generation
Q_w – heat transfer amount
Q_m – mass transfer amount
q_r – radiative heat flux $\left[Wm^{-2}\right]$
q^* – heat generation
Rd – radiation
Re – Reynold's number
Sc – Schmidt number
Sh – Sherwood number
T – dimensional temperature $\left[K\right]$
T_w – wall temperature $\left[K\right]$
T_∞ – ambient temperature $\left[K\right]$
U – free stream velocity $\left[ms^{-1}\right]$

u – velocity in z-direction $\left[ms^{-1}\right]$

U_w – stretching velocity $\left[ms^{-1}\right]$

v – velocity in r-direction $\left[ms^{-1}\right]$

α_f – thermal diffusivity $\left[m^2s^{-1}\right]$

β_T – thermal expansion $\left[K^{-1}\right]$

β_c^* – concentration expansion

δ_1 – velocity slip parameter

δ_2 – thermal slip parameter

δ_3 – concentration slip parameter

η – similarity variable

$\theta(\eta)$ – dimensionless temperature

$\theta'(\eta)$ – rate of temperature change

κ – curvature parameter

μ – dynamic viscosity $\left[kgm^{-1}s^{-1}\right]$

ν – kinematic viscosity $\left[kgm^{-3}\right]$

ρ_f – density $\left[kgm^{-3}\right]$

σ – electrical conductivity $\left[Sm^{-1}\right]$

τ – ratio of nanoparticle effective and base fluid heat capacity

τ_w – shear stress

$\phi(\eta)$ – dimensionless concentration

$\phi'(\eta)$ – rate of concentration

ψ – stream function $\left[m^{-2}s^{-1}\right]$

References

[1] Gersten K. (1998): *Introduction to boundary-layer theory.* In: Kluwick A. (eds) *Recent Advances in Boundary Layer Theory.*– CISM International Centre for Mechanical Sciences, vol.390, pp.1-24, https://doi.org/10.1007/978-3-7091-2518-2_1.

[2] Tulapurkara E.G. (2005): *Hundred years of the boundary layer.*– Sadhana, vol.30, No.4, pp.499-512, https://doi.org/10.1007/BF02703275.

[3] Khan A.U., Ahmed N., Syed T.M., Alsulami M.D. and Khan I. (2022): *A novel analysis of heat transfer in the nanofluid composed by nanodiamond and silver nanomaterials: numerical investigation.*– Scientific Reports, vol.12, No.116, https://doi.org/10.1038/s41598-021-04658-x.

[4] Elbashbeshy E.M.A., Asker H.G. and Nagy B. (2022): *The effects of heat generation absorption on boundary layer flow of a nanofluid containing gyrotactic microorganisms over an inclined stretching cylinder.*– Ain Shams Engineering Journal, vol.13, No.5, No.101690, https://doi.org/10.1016/j.asej.2022.101690.

[5] Eastman J.A., Phillpot S.R., Choi S.U.S. and Keblinski P. (2004): *Thermal transport in nanofluids.*– Annual Review of Materials Research, vol.34, pp.219-246, https://doi.org/10.1146/annurev.matsci.34.052803.090621.

[6] Tuckerman D.B. and Pease R.F.W. (1981): *High-performance heat sinking for VLSI.*– IEEE Electron Device Letters, vol.2, No.5, pp.126-129, https://doi.org/10.1109/EDL.1981.25367.

[7] Elgazery N.S. (2019): *Flow of non-Newtonian magneto-fluid with gold and Alumina nanoparticles through a non-Darcian porous medium.*– Journal of the Egyptian Mathematical Society, vol.27, No.39, https://doi.org/10.1186/s42787-019-0017-x.

[8] Kandasamy R., Muhaimin I. and Mohamad R. (2013): *Thermophoresis and Brownian motion effects on MHD boundary-layer flow of a nanofluid in the presence of thermal stratification due to solar radiation.*– International Journal of Mechanical Sciences, vol.70, pp.146-154, https://doi.org/10.1016/j.ijmecsci.2013.03.007.

[9] Reddy P.S. and Chamkha A.J. (2018): *Heat and mass transfer characteristics of nanofluid over horizontal circular cylinder.*– Ain Shams Engineering Journal, vol.9, No.4, pp.707-716, https://doi.org/10.1016/j.asej.2016.03.015.

[10] Mahdy A. and Chamkha A.J. (2015): *Heat transfer and fluid flow of a non-Newtonian nanofluid over an unsteady contracting cylinder employing Buongiornos model.*– International Journal of Numerical Methods for Heat & Fluid Flow, vol.25, No.3, pp.703-723, https://doi.org/10.1108/HFF-04-2014-0093.

[11] Prasannakumara B.C. (2021): *Numerical simulation of heat transport in Maxwell nanofluid flow over a stretching sheet considering magnetic dipole effect.*– Partial Differential Equations in Applied Mathematics, vol.4, No.100064, https://doi.org/10.1016/j.padiff.2021.100064.

[12] Reddy P.S., Sreedevi P. and Chamkha A.J. (2017): *MHD boundary layer flow, heat and mass transfer analysis over a rotating disk through porous medium saturated by Cu-water and Ag-water nanofluid with chemical reaction.*– Powder Technology, vol.307, pp.46-55, https://doi.org/10.1016/j.powtec.2016.11.017.

[13] Chamkha A.J., Dogonchi A.S. and Ganji D.D. (2019): *Magneto-hydrodynamic flow and heat transfer of a hybrid nanofluid in a rotating system among two surfaces in the presence of thermal radiation and joule heating.*– AIP Advances, vol.9, No.2, No.025103, https://doi.org/10.1063/1.5086247.

[14] Chamkha A.J. and Krishna V.M. (2019): *Hall and ion slip effects on MHD rotating boundary layer flow of nanofluid past an infinite vertical plate embedded in a porous medium.*– Results in Physics, vol.15, No.102652, https://doi.org/10.1016/j.rinp.2019.102652.

[15] Bhatti M. and Abdelsalam S.I. (2021): *Bio-inspired peristaltic propulsion of hybrid nanofluid flow with Tantalum (Ta) and Gold (Au) nanoparticles under magnetic effects.*– Waves in Random and Complex Media, vol.33, No.3, pp.884-904, https://doi.org/10.1080/17455030.2021.1998728.

[16] Hussain S., Mehmood K. and Sagheer M. (2016): *MHD mixed convection and entropy generation of water-alumina nanofluid flow in a double lid-driven cavity with discrete heating.*– Journal of Magnetism and Magnetic Materials, vol.419, pp.140-155, https://doi.org/10.1016/j.jmmm.2016.06.006.

[17] Hussain S., Ahmad S., Mehmood K. and Sagheer M. (2017): *Effects of inclination angle on mixed convective nanofluid flow in a double lid-driven cavity with discrete heat sources.*– International Journal of Heat and Mass Transfer, vol.106, pp.847-860, https://doi.org/10.1016/j.ijheatmasstransfer.2016.10.016.

[18] Globe S. (1959): *Laminar steady state magnetohydrodynamic flow in an annular channel.*– Physics of Fluids, vol.2, No.4, pp.404-407, https://doi.org/10.1063/1.1724410.

[19] Kumar V., Madhukesh J.K., Jyothi A.M., Prasannakumara B.C., Ijaz M.K. and Yu-Ming C. (2021): *Analysis of single and multi-wall carbon nanotubes (SWCNT/MWCNT) in the flow of Maxwell nanofluid with the impact of magnetic dipole.*– Computational and Theoretical Chemistry, vol.1200, No.113223, https://doi.org/10.1016/j.comptc.2021.113223.

[20] Makinde O.D., Khan W.A. and Khan Z.H. (2013): *Buoyancy effects on MHD stagnation point flow and heat transfer of a nanofluid past a convectively heated stretching/shrinking sheet.*– International Journal of Heat and Mass Transfer, vol.62, pp.526-533, https://doi.org/10.1016/j.ijheatmasstransfer.2013.03.049.

[21] Khan W.A., Makinde O.D. and Khan Z.H. (2014): *MHD boundary layer flow of a nanofluid containing gyrotactic microorganisms past a vertical plate with Navier slip.*– International Journal of Heat and Mass Transfer, vol.74, pp.285-291, https://doi.org/10.1016/j.ijheatmasstransfer.2014.03.026.

[22] Vishnu G.N., Ganga B. and Hakeem A.K.A. (2014): *Lie symmetry group analysis of magnetic field effects on free convective flow of a nanofluid over a semi infinite stretching sheet.*– Journal of the Egyptian Mathematical Society, vol.22, No.2, pp.304-310, https://doi.org/10.1016/j.joems.2013.08.003.

[23] Vishnu G.N., Hakeem A.K.A., Jayaprakash R. and Ganga B. (2014): *Analytical and numerical studies on hydromagnetic flow of water based metal nanofluids over a stretching sheet with thermal radiation effect.*– Journal of Nanofluids, vol.3, No.2, pp.154-161, https://doi.org/10.1166/jon.2014.1084.

[24] Rashidi M.M., Vishnu G.N., Hakeem A.K.A. and Ganga B. (2014): *Buoyancy effect on MHD flow of nanofluid over a stretching sheet in the presence of thermal radiation.*– Journal of Molecular Liquids, vol.198, pp.234-238, https://doi.org/10.1016/j.molliq.2014.06.037.

[25] Abbas N., Nadeem S., Saleem A., Malik M.Y., Issakhov A. and Alharbi F.M. (2021): *Models base study of inclined MHD of hybrid nanofluid flow over nonlinear stretching cylinder.*– Chinese Journal of Physics, vol.69, pp.109-117, https://doi.org/10.1016/j.cjph.2020.11.019.

[26] Umeshaiah M., Madhukesh J., Khan U., Rana S., Zaib A., Raizah Z. and Galal A.M. (2022): *Dusty nanoliquid flow through a stretching cylinder in a porous medium with the influence of the melting effect.*– Processes, vol.10, No.6, No.1065, https://doi.org/10.3390/pr10061065.

[27] El-Zahar E.R., Rashad A.M., Saad W. and Seddek L.F. (2020): *Magneto-hybrid nanofluids flow via mixed convection past a radiative circular cylinder.*– Scientific Reports, vol.10, No.10494, https://doi.org/10.1038/s41598-020-66918-6.

[28] Pak B.C. and Cho Y. (1998): *Hydrodynamic and heat transfer study of dispersed fluids with submicron metallic oxide particle.*– Experimental Heat Transfer, vol.11, No.2, pp.151-170, https://doi.org/10.1080/08916159808946559.

[29] Ahmad S. and Pop I. (2010): *Mixed convection boundary layer flow from a vertical flat plate embedded in a porous medium filled with nanofluids.*– International Communications in Heat and Mass Transfer, vol.37, No.8, pp.987-991, https://doi.org/10.1016/j.icheatmasstransfer.2010.06.004.

[30] RamReddy Ch., Murthy P.V.S.N., Chamkha A.J. and Rashad A.M. (2013): *Soret effect on mixed convection flow in a nanofluid under convective boundary condition.*– International Journal of Heat and Mass Transfer, vol.64, pp.384-392, https://doi.org/10.1016/j.ijheatmasstransfer.2013.04.032.

[31] Rashad A.M., Chamkha A.J. and Modather M. (2013): *Mixed convection boundary-layer flow of a nanofluid from a horizontal circular cylinder embedded in a porous medium under convective boundary condition.*– Computers & Fluids, vol.86, pp.380-388, https://doi.org/10.1016/j.compfluid.2013.07.030.

[32] Rashad A.M. and Nabwey H.A. (2019): *Gyrotactic mixed bioconvection flow of a nanofluid past a circular cylinder with convective boundary condition.*– Journal of the Taiwan Institute of Chemical Engineers, vol.99, pp.9-17, https://doi.org/10.1016/j.jtice.2019.02.035.

[33] Rashad A.M., Khan W.A., EL-Kabeir S.M.M. and EL-Hakiem A.M.A. (2019): *Mixed convective flow of micropolar nanofluid across a horizontal cylinder in saturated porous medium.*– Applied Sciences, vol.9, No.23, No.5241, https://doi.org/10.3390/app9235241.

[34] Turkyilmazoglu M. and Pop I. (2013): *Heat and mass transfer of unsteady natural convection flow of some nanofluids past a vertical infinite flat plate with radiation effect.*– International Journal of Heat and Mass Transfer, vol.59, pp.167-171, https://doi.org/10.1016/j.ijheatmasstransfer.2012.12.009.

[35] Anwar T., Kumam P., Shah Z., Watthayu W. and Thounthong P. (2020): *Unsteady radiative natural convective MHD nanofluid flow past a porous moving vertical plate with heat source/sink.*– Molecules, vol.25, No.4, No.854, https://doi.org/10.3390/molecules25040854.

[36] Reddy Y.D. and Shankar B.G. (2023): *Comprehensive analysis of thermal radiation impact on an unsteady MHD nanofluid flow across an infinite vertical flat plate with ramped temperature with heat consumption.*– Results in Engineering, vol.17, No.100796, https://doi.org/10.1016/j.rineng.2022.100796.

[37] Tayabi T., Chamkha A.J., Melaibari A.A. and Raouache E. (2021): *Effect of internal heat generation or absorption on conjugate thermal free convection of a suspension of hybrid nanofluid in a portioned circular annulus.*– International Communications in Heat and Mass Transfer, vol.126, No.105397, https://doi.org/10.1016/j.icheatmasstransfer.2021.105397.

[38] Hafeez A. and Khan M. (2021): *Flow of Oldroyd-B fluid caused by a rotating disk featuring the Cattaneo-Christof theory with heat generation/absorption.*– International Communications in Heat and Mass Transfer, vol.123, No.105179, https://doi.org/10.1016/j.icheatmasstransfer.2021.105179.

[39] Masood S., Farooq M. and Anjum A. (2021): *Influence of heat generation/ absorption and stagnation point on polystyrene-TiO2/H2O hybrid nanofluid flow.*– Scientific Reports, vol.11, No.22381, https://doi.org/10.1038/s41598-021-01747-9.

[40] Turkyilmazoglu M. (2011): *Multiple solutions of heat and mass transfer of MHD slip flow for the viscoelastic fluid over a stretching sheet.*– International Journal of Thermal Sciences, vol.50, No.11, pp.2264-2276, https://doi.org/10.1016/j.ijthermalsci.2011.05.014.

[41] Turkyilmazoglu M. (2012): *Dual and triple solutions for MHD slip flow of non-Newtonian fluid over a shrinking surface.*– Computers & Fluids, vol.70, pp.53-58, https://doi.org/10.1016/j.compfluid.2012.01.009.

[42] Akbar N.S., Khan Z.H. and Nadeem S. (2014): *Copper nanoparticle analysis for peristaltic flow in a curved channel with heat transfer characteristics.*– European Physical Journal Plus, vol.129, No.149, https://doi.org/10.1140/epjp/i2014-14149-4.

[43] Mustafa M. and Khan J.A. (2017): *Numerical study of partial slip effects on MHD flow of nanofluids near a convectively heated stretchable rotating disk.*– Journal of Molecular Liquids, vol.234, pp.287-295, https://doi.org/10.1016/j.molliq.2017.03.087.

[44] Mahanthesh B., Mabood F., Gireesha B.J. and Gorla R.S.R. (2017): *Effects of chemical reaction and partial slip on the three-dimensional flow of a nanofluid impinging on an exponentially stretching surface.*– European Physical Journal Plus, vol.132, No.3, No.142, https://doi.org/10.1140/EPJP/2017-11389-8.

[45] Pradhan S.R., Baag S., Mishra S.R. and Acharya M.R. (2019): *Squeezing flow analysis of MHD micropolar fluid on radial and angular velocity: A semianalytical approach.*– Heat Transfer-Asian Research, vol.48, No.6, pp.2799-2818, https://doi.org/10.1002/htj.21515.

[46] Mishra S.R., Pattnaik P.K., Baithalu R., Ratha P.K. and Panda S. (2024): *Predicting heat transfer performance in transient flow of CNT nanomaterials with thermal radiation past a heated spinning sphere using an artificial neural network: A machine learning approach.*– Partial Differential Equations in Applied Mathematics, vol.12, No.100936, https://doi.org/10.1016/j.padiff.2024.100936.

[47] Agbaje T.M., Baithalu R., Mishra S.R. and Panda S. (2024): *Irreversibility Processes on the Squeezing Flow Analysis of Blood-Based Micropolar Hybrid Nanofluid Through Parallel Channel: Spectral Quasilinearization Method.*– BioNanoScience, vol.14, pp.3226-3240, https://doi.org/10.1007/s12668-024-01417-w.

[48] Panda S., Pattnaik P.K., Baithalu R. and Mishra S.R. (2024): *Inertial drag combined with non-uniform heat generation/absorption effects on the hydromagnetic flow of polar nanofluid over an elongating permeable surface due to the impose of chemical reaction.*– ZAMM - Journal of Applied Mathematics and Mechanics, vol.104, No.7, No.e202301058, https://doi.org/10.1002/zamm.202301058.

[49] Mabood F. and Shateyi S. (2019): *Multiple slip effects on MHD unsteady flow heat and mass transfer impinging on permeable stretching sheet with radiation.*– Modelling and Simulation in Engineering, vol.2019, No.3052790, https://doi.org/10.1155/2019/3052790.

[50] Rosseland S. (1931): *Astrophysik und Atom-Theoretische Grundlagen.*– Springer-Verlag, Berlin, vol.41, https://doi.org/10.1007/978-3-662-26679-3-3.

[51] Abdel-Wahed M.S. and El-Said E.M. (2019): *Magnetohydrodynamic flow and heat transfer over a moving cylinder in a nanofluid under convective boundary conditions and heat generation.*– Thermal Science, vol.23, No.6A, pp.3785-3796, https://doi.org/10.2298/TSCI170911279A.

[52] Nadeem S., Ul Haq R. and Akbar N.S. (2014): *MHD three-dimensional boundary layer flow of Casson nanofluid past a linearly stretching sheet with convective boundary condition.*– IEEE Transactions on Nanotechnology, vol.13, No.1, pp.109-115, https://doi.org/10.1109/TNANO.2013.2293735.

Received: August 16, 2025
Revised: January 28, 2026